Proton-induced traps in electron multiplying charge-coupled devices

Proton-induced traps in electron multiplying charge-coupled devices

Nathan Bush,* David Hall, and Andrew Holland
The Open University, Department of Physical Sciences, Milton Keynes, United Kingdom

Abstract. Charge-coupled device (CCD)-based technologies exposed to high-energy radiation are susceptible to the formation of stable defects within the charge transfer channel that defer signal to subsequent pixels and limit the lifetime of the detector. Performance degradation due to these defects depends upon the interplay between the clock timings used to operate the device and the properties of defects introduced by irradiation. Characterization of both the type and number of post-irradiation defects makes it possible to minimize charge loss though the appropriate selection of clock timings for a given operating temperature. This technique has the potential to increase nominal mission lifetimes by several years for CCD-based instruments and is of particular significance to electron multiplying charge-coupled devices (EMCCDs) for photon counting applications where the effect of charge traps on low signal levels is expected to be most severe. We present a study of charge traps within CCDs, specifically within EMCCDs irradiated at room temperature to proton fluences up to and including 1.45×10^{10} p^{+}/cm^{2} (74 MeV). Defects are characterized through the "single-trap pumping" technique, with clocking schemes specifically designed for the 2-phase pixel architecture of the EMCCD. Five dominant trap species are thought to be introduced by the irradiation, the Si-E center, Si-A center, double and single acceptor charge states of the silicon divacancy (VV^{--}, VV^{-}), and an as yet unidentified defect referred to here as the Si-U center (the "unknown" trap). Energy-level and cross-section values are presented that allow inference of the defect landscape for a range of proton fluences and operating temperatures. While the study focuses specifically on EMCCDs, in more general terms, the results for trap properties are interpreted as being applicable to all CCD types following irradiation and can serve as a foundation for future charge loss correction and optimization techniques. [DOI: 10.1117/1.JATIS.7.1.016003]

Keywords: electron multiplying charge-coupled devices; charge-coupled devices; silicon defects; charge traps; trap pumping; CTE; charge transfer inefficiency.

Paper 20126 received Aug. 23, 2020; accepted for publication Jan. 20, 2021; published online Mar. 9, 2021.

1 CCDs within the Space Environment

Electron multiplying charge-coupled devices (EMCCDs) are a variant of standard charge-coupled device (CCD) technology that permits single photon detection through use of an in-built gain mechanism that amplifies signals above the read noise of the output amplifier.[1] This is achieved through the inclusion of an electron multiplication (EM) register that is appended to the standard serial register and connected to its own output. The device otherwise functions similarly to a standard CCD, with an image area, frame store, and conventional output amplifier (Fig. 1). Operation at high EM gain (>1000) and low incident photon flux (<0.1 photons/pixel/frame) in conjunction with a thresholding technique ($\approx 5\sigma$) permits detection of single optical photons with near-perfect detection efficiency.[2,3] The technology has been widely adopted for ground-based applications and is now being implemented within space instruments such as the Roman Space Telescope (formerly WFIRST) coronagraph instrument.[4] Variants of the technology are also under consideration for future astronomy missions, such as the Habitable Exoplanet Observatory (HabEx) and the Large UV/Optical/IR Surveyor.[5,6]

*Address all correspondence to Nathan Bush, Nathan.Bush@jpl.nasa.gov

2329-4124/2021/$28.00 © 2021 SPIE

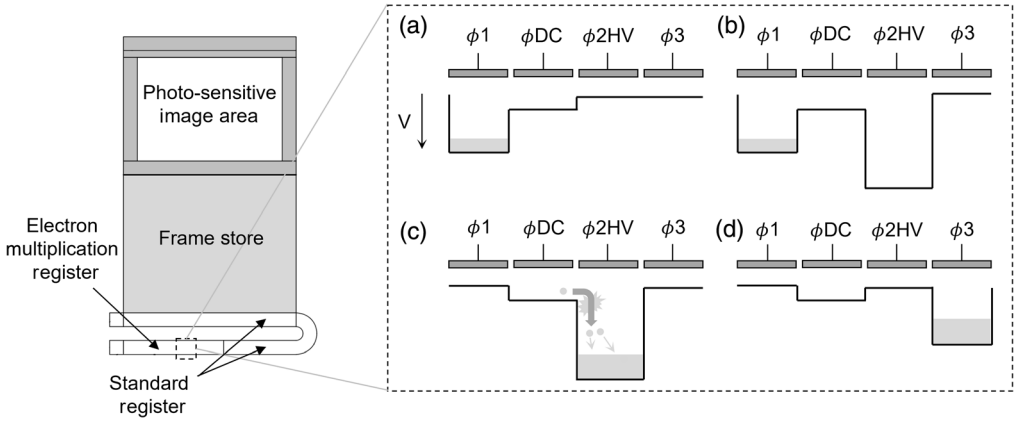

Fig. 1 Schematic of an EMCCD, with an enlarged view of an EM register pixel structure and clocking sequence. The pixels contain two phases specialized for the generation of a high electric field that accelerates carriers to energies necessary for impact ionization to occur, amplifying the signal. ϕDC is biased at a fixed value between 3 and 5 V, whereas Rϕ2HV has a timed high-voltage pulse applied in the range 12 to 45 V depending upon the required EM gain. Clocking sequence: (a) charge stored beneath Rϕ1, (b) Rϕ2HV pulse is applied, (c) Rϕ1 pulse low, charge moves beneath ϕDC and experiences high field and (d) charge transferred to Rϕ3, ready to transfer to the next EM element.

For space-based applications, the technology is susceptible to radiation damage from high-energy particles that degrade electro-optical performance and limit the lifetime of the detector. EMCCDs function identically to CCDs in the sense that signal packets must be transferred sequentially toward the output pixel by pixel along a total distance that often totals a few centimeters. This requirement makes the devices inherently vulnerable to the presence of bulk traps within the charge transfer channel. An increase in the density of these traps manifests as an increase in the measured charge transfer inefficiency (CTI $= 1 -$ CTE) of the device, resulting in loss of the leading edge of signal and the presence of a "tail" in both parallel and serial directions (Fig. 2). Since charge loss is a subtractive process, the effect is most severe for smaller signal sizes such as those relevant to EMCCDs. Space-based implementations of the technology

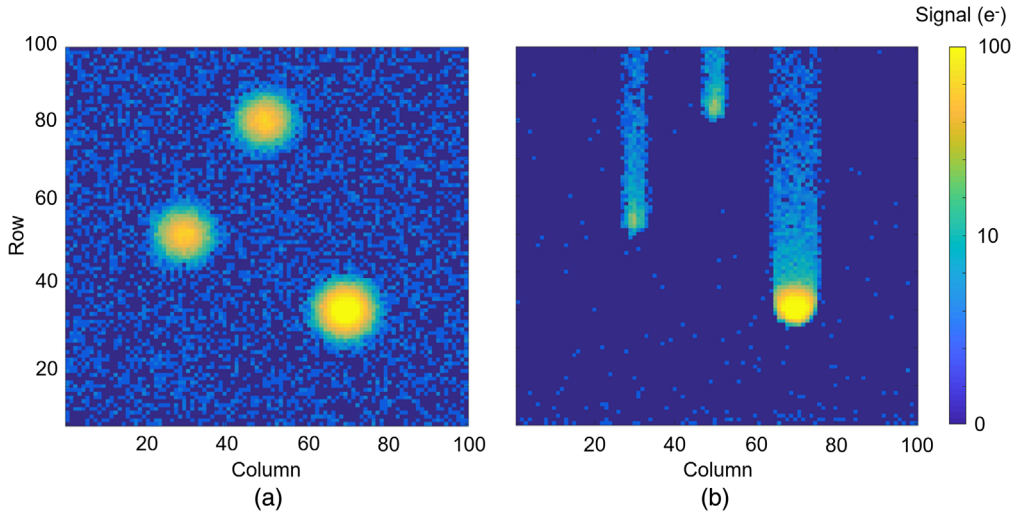

Fig. 2 Simulation of the effect of charge traps on parallel transfer within summed photon counted images. (a) An undamaged, summed photon counted image for three-point sources. The lower right source is 5 times as bright as the other two. (b) The effect of charge traps is to subtract charge from the leading edge of the signal and add a "tail" in the direction of transfer. This simulation highlights the effect of parallel CTI only and used an artificial defect distribution to highlight the presence of parallel charge tails.

are therefore set to benefit from a detailed catalog of the defects that form due to irradiation since this information can inform both optimization and correction strategies that can increase the useful detector lifetime. The aim of this study was to catalog the number and properties of defects produced in EMCCDs as result of high-energy (74 MeV) proton irradiation to provide information that would act as a firm foundation for future mitigation techniques. The underlying theory for defect formation is discussed, followed by the experimental techniques used to study the defects. The results of the defect catalog process are presented in terms of number density, energy levels, and cross sections. This information can be used to infer the post-irradiation defect landscape and estimate, reduce, and correct for CTI across a wide range of instrument operating temperatures and clock timings.

2 Defect Formation in EMCCDs

The majority of the damage to a CCD-based instrument within a space environment such as $L2$ is due to high-energy solar protons.[7] As protons pass through an EMCCD, they deposit energy through both ionising and non-ionising energy loss (NIEL). NIEL encompasses lattice displacements that can occur through Coulomb interactions ($E_P \leq 10$ MeV), elastic or inelastic nuclear scattering.[8] For each interaction, a fraction of the incident proton energy is transferred to a silicon atom. A displacement occurs when the energy transfer is greater than the threshold energy ($E_d \approx 25$ eV[9]), at which point there is an interstitial silicon atom and a vacancy, together referred to as a Frenkel pair. The first displaced atom (the interstitial) is also referred to as the primary knock-on atom (PKA) and has kinetic energy remaining from the collision. PKAs with energy below the threshold energy cannot form additional displacements. In this case, the damage is limited to an isolated Frenkel pair that may recombine, leaving no net damage, or migrate throughout the lattice to form other point defects. PKAs with enough energy displace additional silicon atoms resulting in damage cascades and defect clusters. Low-energy proton interactions (≤10 MeV) predominantly result in point defects.[8] As the proton energy increases above this point, the dominant interaction mechanism switches to nuclear interactions and defect clusters become more common. For the case of an astronomy mission with moderate shielding (10 to 40 mm of Al or equivalent), the mode proton energy can range from 30 to 70 MeV with an energy spectrum that extends to a few hundred MeV (Fig. 3). The silicon defect landscape for such a mission shall consist of mainly point defects with a small fraction of clusters with potential to capture larger signals. Not captured within Fig. 3 are the secondary particles generated through interaction of primary protons and the shielding material. The secondary particle

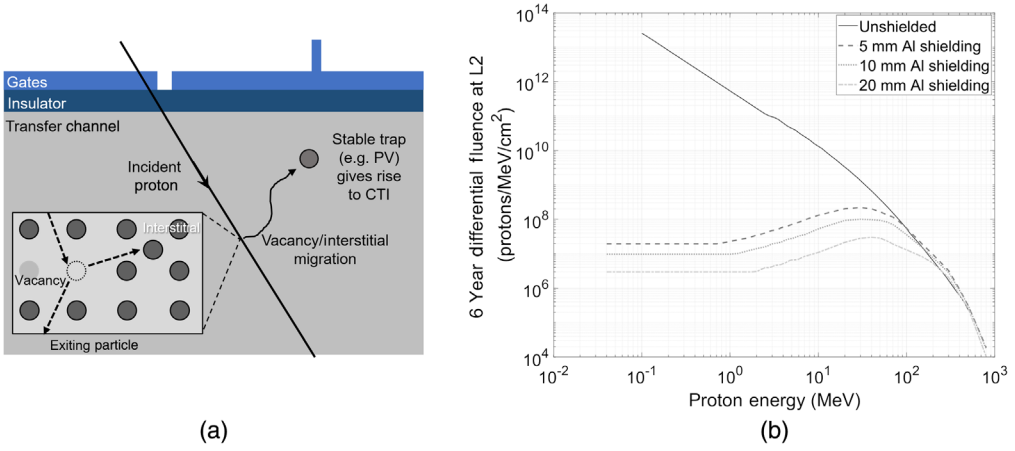

Fig. 3 (a) Cross section of a CCD pixel showing an interaction between an energetic proton and the silicon lattice of the detector. The primary interaction can result in a Frenkel pair. The vacancy and interstitial then migrate through the lattice and combine with other impurities to form stable defects. (b) Unshielded and shielded *L2* proton fluence for different degrees of aluminum shielding. Increasing the thickness or mass beyond 40 mm Al equivalent is rarely practical, and even with this level of shielding protons with energy ≥100 MeV still reach the detector.

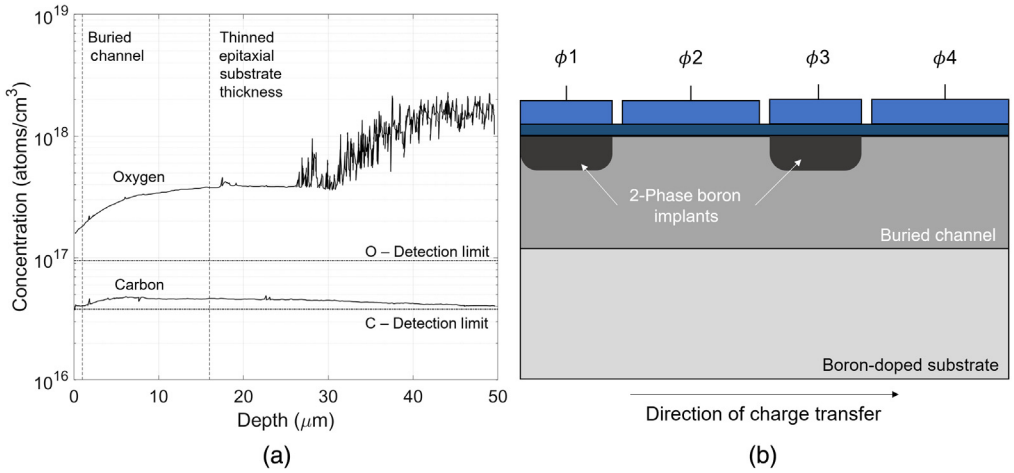

Fig. 4 (a) SIMS analysis of a processed CCD wafer with epitaxial thickness of 16 μm. To avoid thick gate layers, the ion etch took place near to the wafer's edge. (b) Schematic of a CCD pixel with 2-phase implants labeled. The implant shape and depth are for illustration purposes only and may not be accurate. The buried channel is phosphorus doped and extends approximately 1 μm into the device. Charge storage and transfer typically occur approximately 0.5 μm into the device.[11]

spectrum may constitute a non-negligible component of the total damage and impact the ratio of point defects to clusters. For this investigation, point defects with single electron occupancy remained the focus since they are expected to dominate charge loss for most applications.

The defect species that form depend upon the dopants and impurities present within the EMCCD starting silicon. Thin ($\leq$40 μm) EMCCDs are manufactured using epitaxial material grown on a Czochralski (Cz) substrate. Since the growth process occurs at high temperature ($\approx$900°C to 1000°C), impurities from the Cz substrate diffuse into the epitaxial material.[10] Oxygen and carbon are thought to dominate and are expected in concentrations ranging from 1×10^{17} to 5×10^{17} atoms/cm^3 and 5×10^{15} to 1×10^{16} atoms/cm^3, respectively (Fig. 4). The formation of the buried channel involves the introduction of an N-type donor atom, typically phosphorus, through ion implantation. The concentration is described by a Fick diffusion profile and is typically of the order 10^{16} atoms/cm^3 at the charge storage location within the channel.[11,12] The substrate is also P-doped with boron, giving an estimated background concentration of approximately 10^{15} atoms/cm^3 based upon the known resistivity of 20 Ω.cm.[13] Additional implants are sometimes introduced according to the device architecture. An example specific to the EMCCD is the additional boron implants added to define the "two phase" clocking potential.[14] These implants cause a distortion in the electronic potential of order a few V, and so the concentration of boron in these regions is expected to be lower than that for the buried channel but higher than the background concentration.

The defects that can form within the transfer channel of EMCCDs are therefore primarily limited to complexes between oxygen, phosphorus, carbon, boron, and the stable combinations of vacancies and interstitials. For a defect to be a charge trap, it must have an energy level between silicon valence and conduction band. Of these, its defects that have acceptor levels in the upper half of the bandgap that can degrade CTE. Table 1 summarizes defects that could potentially impact charge transfer performance in EMCCDs, based upon the selection criteria outlined through this discussion.

While the list of possible defects is long, only a few are expected to dominate post-irradiation performance. The potential impact is dependent upon the number density and the emission time constant of the trap (τ_e), which itself is a function of the defect emission cross section (σ_p), energy level (E), and the operating temperature of the device (T).[25,26]

$$\tau_e = \frac{1}{\sigma_p N_C v_{\text{th}}} e^{\frac{E}{k_B T}}, \tag{1}$$

Table 1 Summary of defects capable of impacting charge transfer performance within EMCCDs based on the discussion of impurities within epitaxial silicon. Species that have been found within Teledyne-e2v CCDs within previous studies are highlighted in bold. The list may not be exhaustive. It was not possible to identify cross-section values for some defects; however, unquoted values are likely to be within the range 10^{-14} to 10^{-16} cm^2 based upon the configuration and charge state. The values listed for the same defect within different references differ slightly, preference was given to any investigations where the parameters were measured directly in CCDs. The first listed reference is where the value was obtained from.

Description	Symbol	$E_C - E$ (eV)	σ_p (cm^2)	Refs.
Divacancy (double acceptor) VV^{--}	VV$^{--/-}$	−0.235	1.35×10^{-15}	14–16
Divacancy (single acceptor) VV^{-}	VV$^{-/0}$	−0.420	1.5×10^{-15}	15, 16
Self-interstitial-oxygen interstitial	$Si_iO_i^-$	−0.390	—	16, 17
Vacancy-oxygen interstitial (Si-A)	$VO_i^{(-/0)}$	−0.165	6.1×10^{-15}	15, 16, 18
Boron interstitial	B_i^-	−0.45	—	16, 19
Boron interstitial oxygen interstitial	$B_iO_i^{(-/0)}$	−0.27	1.2×10^{-15}	16, 20
Phosphorus vacancy (PV, Si-E)	PV$^{(-/0)}$	−0.456	3.7×10^{-15}	16, 21
Carbon interstitial–carbon substitutional	$C_iC_s^-$ (A$^-$)	−0.17	—	16, 22
Carbon interstitial–phosphorus substitutional	$C_iP_s^-$ (IA)	−0.38	—	16, 23
Carbon interstitial–phosphorus substitutional	$C_iP_s^-$ (IB)	−0.39	—	16, 23
Carbon interstitial–phosphorus substitutional	$C_iP_s^-$ (IIA)	−0.26	—	16, 23
Carbon interstitial–phosphorus substitutional	$C_iP_s^-$ (IIB)	−0.31	1.5×10^{-14}	14, 16, 23
Carbon interstitial–phosphorus substitutional	$C_iP_s^-$ (III)	−0.23	3.0×10^{-15}	14, 16, 23
"Unknown"	—	−0.345	5.0×10^{-16}	24

where N_C is the density of states in the conduction band, k_B is the Boltzmann constant, and v_{th} is the thermal velocity of the electron, discussed within the Appendix. When a charge packet encounters a trap, it must first be captured, following which there is an amount of time where the trap may release its charge such that it re-joins the original signal packet. If the trap emits during this time, then there is no net charge loss. If the trap emits after this time, then the signal is emitted into a later pixel and the trap contributes to net charge loss.

Figure 5 shows the emission time constant of the dominant species described found within previous studies of Teledyne-e2v CCDs as a function of temperature. Parallel EMCCD timings range between 10^{-6} and 10^{-2} s, serial timings can vary from 10^{-9} to 10^{-6} s, and single frame integration times can exceed 10^2 s, and so the dominant defects will vary considerably depending upon operating conditions. Slower operation of the EMCCD provides additional opportunity for recently captured charge to be re-emitted into the original signal packet. However, it also provides time for occupied traps that are between the packet and the output node to empty. Intelligent optimization must focus on keeping as many traps filled as possible while also allowing as many traps to re-emit into the original signal packet, i.e., minimizing the number of effective traps. To achieve this, knowledge of the emission time constants of every defect as a function of temperature is required alongside the relative abundance of each species so that the dominant traps are given more weight during optimization of clocking. A catalog of the defects present within an irradiated EMCCD can therefore be used to minimize the number of effective traps and hence optimize CTE for any range of operating conditions of the EMCCD. While this study is specifically focused on the EMCCD, the technique is applicable to any device that exhibits the CCD transfer-reliant architecture that is vulnerable to bulk trap formation.

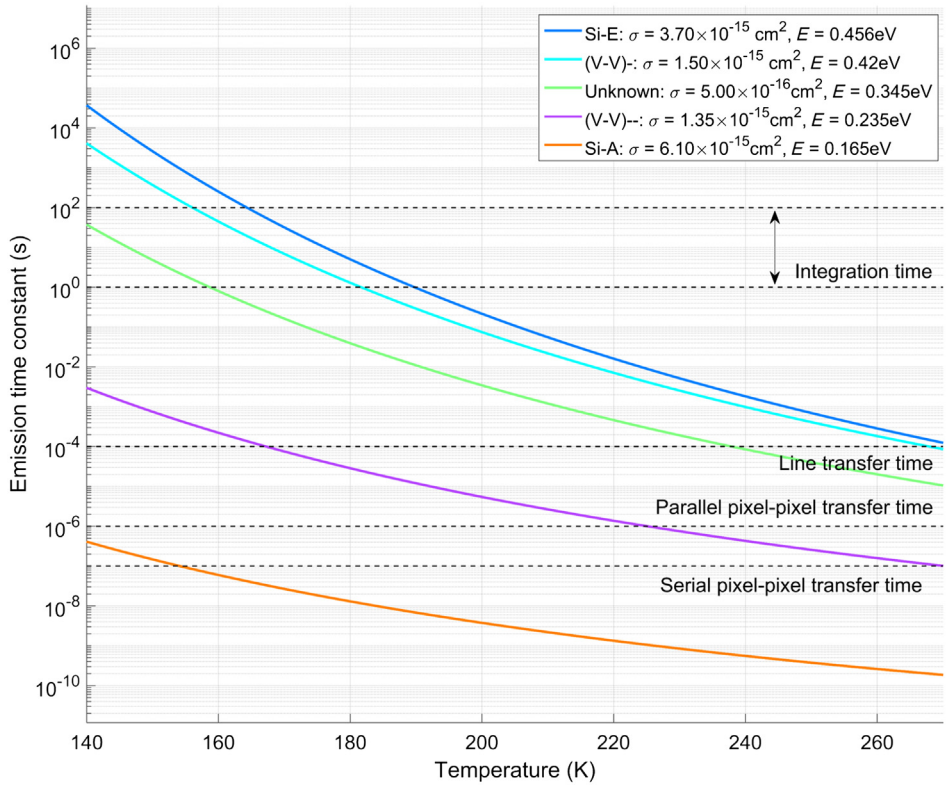

Fig. 5 Plot of emission time constant (τ_e) versus temperature for defects identified in N-channel CCDs following irradiation, with parameters taken from Table 1. Example EMCCD operating timings have been overlaid to illustrate how each of the defects may influence each aspect of device performance. The line transfer time is defined as the time taken to read out a line of the CCD, and so has dependence on the serial frequency and frame size. 0.1 to 1 ms is typical. The parallel and serial transfer times are defined as the time taken to transfer charge from one pixel to the next. Typical operating temperatures for space-based CCD and EMCCD instruments are within the range 150 to 200 K.

3 Probing Silicon Defects within EMCCDs

The space heritage of CCD-based instruments now spans over three decades and so many studies exist that focus on the nature of charge traps and mitigation techniques such as optimized clock timings, charge loss correction algorithms, and high-temperature annealing.[27–30] Until recently, however, the properties of many defects have been inferred from measurements of CTI as a function of temperature. While these techniques remain useful, they are susceptible to interference from systematic electronic effects and provide the averaged effect of trapping sites the signal encounters under specific operating condition. A catalog of individual trap properties allows CTE optimization over a range of operating conditions through calculation of the emission time constant at a specific temperature. Furthermore, this information can provide a more accurate prediction of the effect of a signal profile as it is transferred to the output. The "single trap pumping" technique allows characterization of individual defects within the transfer channel of the device, providing information on their precise location, emission time constant, energy level, and cross section. [31–37] A detailed description of the development of the underlying theory can be found within Ref. 18, and Ref. 14 for the case of EMCCDs, and so only a summary is included here.

The technique involves a flat field of illumination being clocked between phases within a pixel such that charge can be repeatedly captured by a trapping site and then emitted into a neighboring pixel. Each step of the clocking scheme is separated by a controllable time, referred as the phase time (t_{ph}), that is typically constant for each step in the scheme. If a trap is present with an emission time constant (τ_e) comparable to the phase time, charge may be "pumped" from

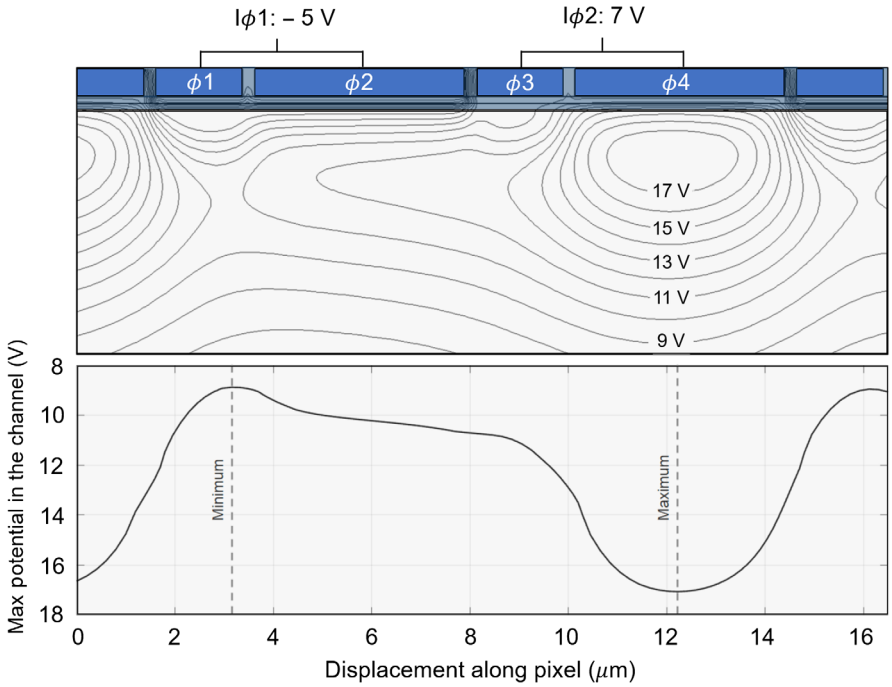

Fig. 6 TCAD simulation of a CCD201 image pixel at datasheet voltages using 2-phase clock pairings, taken and modified from Ref. 14.

one pixel to another. The repetition of this process over numerous (≈10000) cycles gives rise to a bright dark pixel pattern referred to as a "dipole." Measurements of the intensity of the dipole at a given temperature as a function of t_{ph} give rise to a curve of the form:

$$I(t_{\mathrm{ph}}) = NP_P, \tag{2}$$

where N is the number of pumping cycles and P_P is the probability that a trap will pump within a complete clocking cycle. The functional form of P_p is dependent upon the pixel architecture. The Teledyne-e2v CCD201 was chosen for this study. The CCD201 is a $1k \times 1k$ frame transfer device with 13-μm-square image pixels that each have four separately connected electrodes that can be paired to operate with 2-phase clocking if required. Figure 6 shows a schematic of the CCD201 pixel with a SILVACO Technology Computer Aided Design (TCAD) simulation of the potential profile within a pixel during standard 2-phase clocking conditions at datasheet biases.[14]

The precursor to this study used these potential profiles to devise a trap-pumping clocking scheme that probed defects beneath $I\phi 2$ and $I\phi 4$, with different functions describing the intensity of the dipole as a function of phase time depending on the sub-phase location of the trap.[14] It was shown that charge capture beneath the barrier phases ($I\phi 1$ and $I\phi 3$) is negligible for moderate signal sizes and clocking speeds, so this single scheme was adequate to give a measure of the absolute number of traps. However, this single scheme could not be used to calculate the position of a trap within the pixel to high accuracy. Since the impact of the trap is strongly dependent upon the physical location of the defect within the pixel, three additional pumping schemes were developed as part of this study to provide high-resolution location information (Table 2).

Implementation of Schemes 1 to 4 on a CCD201 will result in dipoles that exhibit one of three possible functional forms of P_P depending upon the pumping scheme and the location of the defect [Eqs. (3)–(5)]:

$$P_{P1} = NP_c\left(e^{-\frac{t_{\mathrm{ph}}}{\tau_e}} - e^{-\frac{2t_{\mathrm{ph}}}{\tau_e}}\right), \tag{3}$$

Table 2 Clock pairings used for each of the four trap pumping schemes described within the main text. When information from these schemes is combined, the location of defects can be determined to sub-phase resolution.

Time step	Scheme 1	Scheme 2	Scheme 3	Scheme 4
t_{ph}	$\phi2+\phi3$	$\phi1+\phi2$	$\phi3+\phi4$	$\phi2+\phi3$
$2t_{ph}$	$\phi1+\phi2$	$\phi3+\phi4$	$\phi2+\phi3$	$\phi3+\phi4$
$3t_{ph}$	$\phi3+\phi4$	$\phi1+\phi4$	$\phi1+\phi2$	$\phi1+\phi4$
$4t_{ph}$	$\phi1+\phi4$	$\phi2+\phi3$	$\phi1+\phi4$	$\phi1+\phi2$
$5t_{ph}$	—	—	$\phi1+\phi2$	$\phi1+\phi4$
$6t_{ph}$	—	—	$\phi2+\phi3$	$\phi3+\phi4$

$$P_{P2} = NP_c\left(e^{-\frac{2t_{ph}}{\tau_e}} - e^{-\frac{3t_{ph}}{\tau_e}}\right), \tag{4}$$

$$P_{P3} = NP_c\left(e^{-\frac{t_{ph}}{\tau_e}} - e^{-\frac{4t_{ph}}{\tau_e}}\right). \tag{5}$$

The orientation of the dipole varies according to its location of the trap within the pixel; charge will either be emitted into the pixel to the left or right depending on the phase location and potential profile within the pixel at the time of emission. Figures 7 and 8 show the orientation of each dipole according to the phase location of each trap for each of the four schemes and a plot of each form of P_P, respectively. The use of all four multiple schemes is important to ensure that the correct form of P_P is fitted to each trap. For example, a dipole with positive polarity in Scheme 1 and negative polarity in Schemes 2 and 3 must be located on the RHS of $\phi2$, and should therefore be fitted with P_{p1} for data obtained with Scheme 1, or P_{P3} for data obtained with Scheme 3. Incorrect fitting of P_P to the dipole intensity curve results in an error in the distribution of emission time constants, giving false daughter peaks that complicate analysis.[14,38]

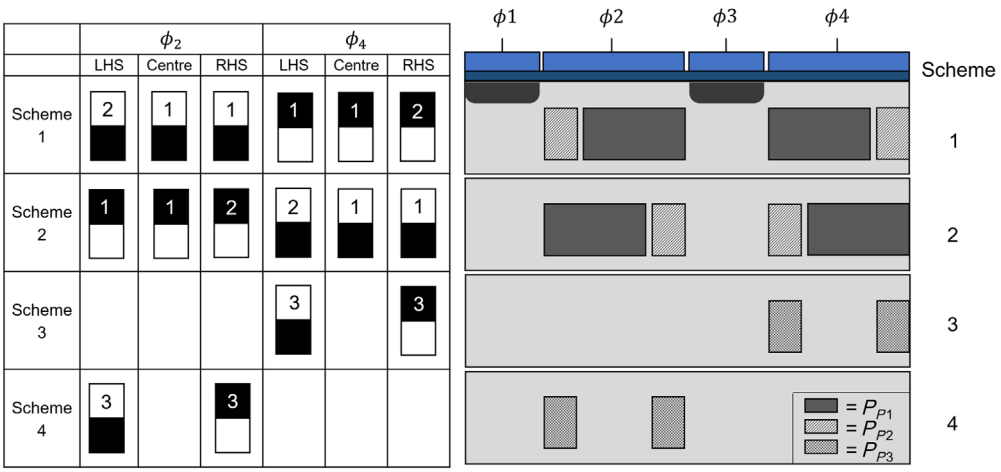

Fig. 7 (a) Diagram showing the orientation of each dipole according to the location of the trap. "Positive" polarity refers to a dipole that has a leading bright pixel, and vice versa. The number indicates the functional form of P_P that applies to each dipole [Eqs. (3)–(5)]. (b) Schematic of a CCD201 pixel showing the regions that each of the P_P functions applies to for each of the four pumping schemes within Table 2.

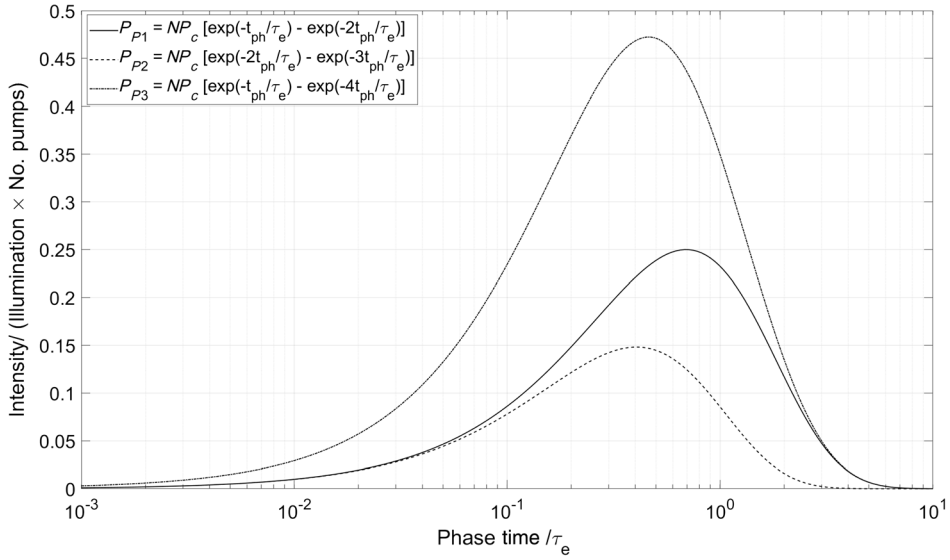

Fig. 8 Summary of the three functions that describe P_P for the trap-pumping schemes described within Table 2. Each function has a different maximum amplitude and peak location.

Each form of P_P [Eqs. (3)–(5)] assumes that temperature is fixed to ensure τ_e is constant throughout the dataset. As the temperature is increased, the emission time constant decreases by a factor dependent on the energy level and cross section of the defect [Eq. (1)]. A fit to τ_e as a function of temperature can return both E and σ_p for the trap; however, care must be taken to ensure the fit is performed correctly; N_C and v_{th} vary as a function of temperature and this must be accounted for. The formulism used in this study is provided in the Appendix and is the same formulism that should be used when interpreting any of the results presented later. Subtle changes in the effective energy level of the trap through different mathematical treatment can manifest as large variations in τ_e. A fit to Eq. (1) also assumes the enthalpy values for the traps do not change with temperature despite bandgap narrowing, i.e., the traps are pinned to the conduction or valence bands. The result of the fit is therefore the energy level with respect to the bandgap edge, which itself shifts as a function of temperature.

Seven commercial CCD201 EMCCDs were studied (Table 3). Three were irradiated at the Paul Scherrer Institut (PSI), Switzerland, another at STERIS, Harwell, UK, and the remaining devices kept as unirradiated controls. The irradiations at PSI were performed at room temperature, unbiased and with shielding to maintain on-chip parallel control regions. The primary beam energy was 74 MeV, and fluences can be normalized to the 10-MeV equivalent using the non-ionizing energy loss (NIEL) function.[8,9,39,40] The irradiation at STERIS was performed with the detector biased, using 5-MeV protons and no shielding.

Table 3 Summary of devices studied and the details of each irradiation

Serial number	Date irradiated	Proton fluence (p^+/cm^2)	Notes
14222-11-2	May 14, 2016	$(2.09 \pm 0.2) \times 10^9$	Irradiated unbiased with a 74-MeV primary beam
10091-16-7	February 23, 2015	$(5.23 \pm 0.52) \times 10^9$	Irradiated unbiased with a 74-MeV primary beam
14222-14-2	December 4, 2015	$(1.45 \pm 0.15) \times 10^{10}$	Irradiated unbiased with a 74-MeV primary beam
15293-15-4	June 29, 2018	$(3.65 \pm 0.37) \times 10^9$	Irradiated biased with a 5-MeV primary beam
11281-22-15	—	—	Unirradiated
14222-20-6	—	—	Unirradiated
12231-21-19	—	—	Unirradiated and no aluminum store shield

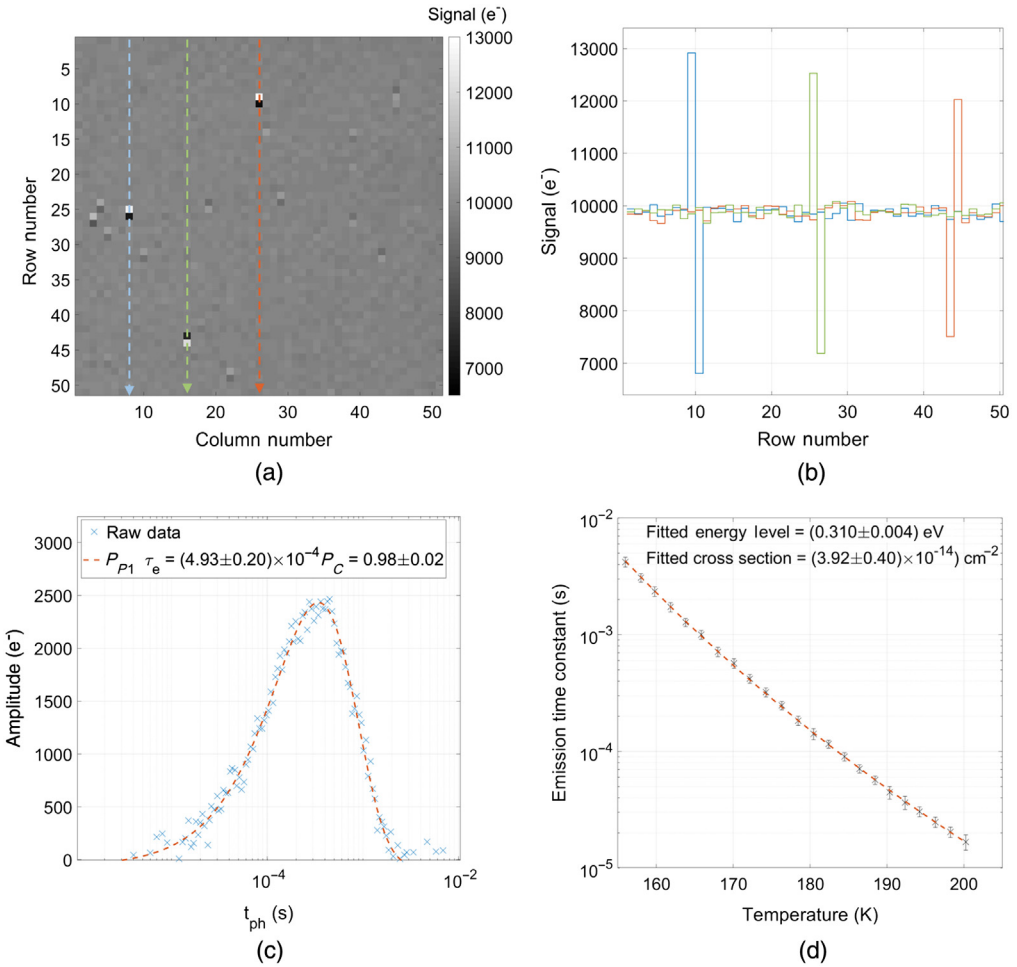

Fig. 9 (a) Image of dipoles following the trap pumping process. (b) Intensity profile of dipoles whereby the rise and subsequent drop in intensity are due to the trapped and released signal over multiple cycles. (c) Dipole tracked as a function of phase time, leading to the form of P_{P1}. (d) Fit to τ_e as a function of temperature, returning an energy level and cross section with associated error.

The trap-pumping technique was implemented using a flat field of approximately 10,000 e$^-$. The number of pumping cycles (N_P) was set to 10,000, giving a maximum pumped signal of 2500 e$^-$ for P_{P1}, assuming a capture probability of 1. Devices were operated at 1 MHz with a read noise of approximately 20 e$^-$, leaving photon shot noise as the dominant noise source. Assuming a 3σ detection threshold, these conditions allowed the intensity curve of a trap to be tracked when the pumping efficiency was $\geq 12\%$ of the peak intensity for the example of P_{P1} ($P_C \geq 12\%$).

Measurements were made in the temperature range of 150 to 240 K in the time-domain spanning 10^{-6} to 10^{-2} s. Faster clocking (> 1 MHz) in the parallel direction was not possible without significant CTE degradation. At the higher temperatures (≥ 220 K), thermal dark signal and hot pixels became an increasing source of data contamination. This was resolved through subtraction of bias frames that were obtained with identical integration times as experienced by the pumped frames, albeit with no pumping taking place. A fixed, low-activity ^{55}Fe source was pointed at the detector for calibration throughout data collection. Defects were identified though use of a 3σ detection threshold, and the intensity of each dipole was tracked as a function of phase time. Dipoles from each pumping scheme were compared so that the correct form of P_P was fitted to return the emission time constant at a given temperature. For each defect, the emission time constant was tracked as a function of temperature and fitted using Eq. (1) to return an energy level and cross section for each identified trap (Fig. 9).

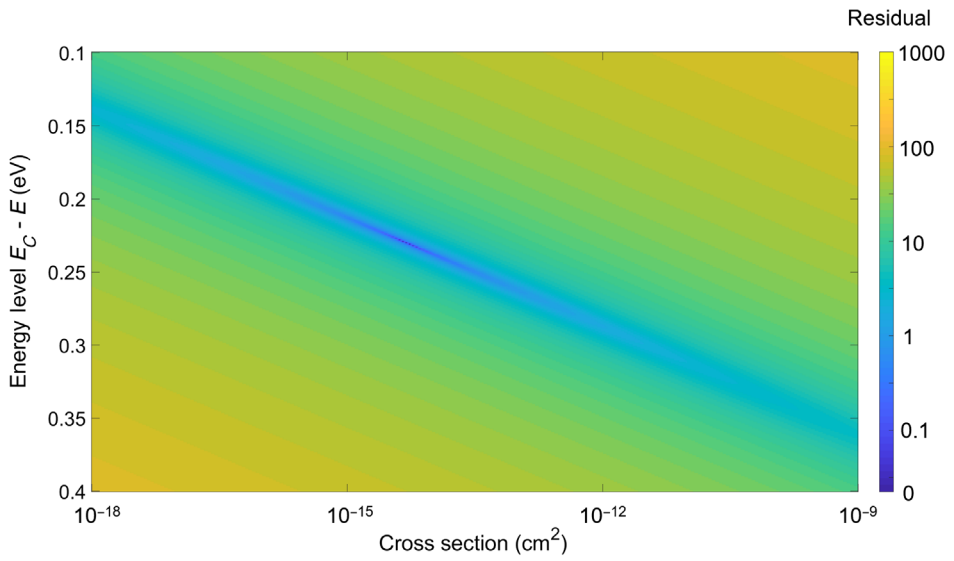

Fig. 10 The energy level and cross section of a trap is returned by fitting Eq. (1) with measured values of τ_e as a function of temperature. Measured values of τ_e have associated error, primarily due to photon shot noise, and this translates into error on the fitted values of E and $\boldsymbol{\sigma}$. The residual is given by the difference between the data and the fit results, and was calculated for simulated values of τ_e as a function of T with 20% error for a trap with $E = 0.23$ eV and $\boldsymbol{\sigma} = 4 \times 10^{-15}$ cm^2. These simulated values were fitted using Eq. (1) and compared to the true value. There is a clear "valley" where the residual drops to low values for certain E and $\boldsymbol{\sigma}$. The shape of the valley is consistent with the function; exponential variation of $\boldsymbol{\sigma}$ can compensate for a linear variation in energy level and return the same emission time constant. The addition of error on τ_e means that the lowest residual will not necessarily be at the true $E/\boldsymbol{\sigma}$ value, but at the point within this valley where the residual is lowest.

The most detailed investigation was performed on device 14222-11-2. This device was irradiated to the lowest fluence (2.09×10^9 p$^+$/cm^2 74 MeV) and exhibited enough defects for analysis without a high likelihood of multiple defects per pixel. Measurements were made using 2-K increments from 156 to 240 K for this device. Additional measurements were made using the remaining devices in targeted areas to highlight any differences in the absolute and relative abundance of trap species as a function of proton fluence.

The amplitude of each dipole has noise that propagates into error on the fitted emission time constant. This in turn results in error on the calculated energy level and cross section. A least-squares minimization procedure was used to fit values of E and $\boldsymbol{\sigma}$ to the measured values for τ_e. This routine varied E and $\boldsymbol{\sigma}$ within a set range to achieve the smallest residual between the fitted function and the real data. Figure 10 shows a plot of the residual as a function of both E and $\boldsymbol{\sigma}$ for some example data. There is a clear "valley" where the residual drops to low values for certain E and $\boldsymbol{\sigma}$. The shape of the valley is consistent with the fitted function; exponential variation of the cross section can compensate for a linear variation in energy level and return the same emission time constant. The addition of error on τ_e means that the lowest residual will not necessarily be at the true $E/\boldsymbol{\sigma}$ value, but at the point within this valley where the residual is lowest. Random error added to otherwise discrete values of E and $\boldsymbol{\sigma}$ results in a spread of energy levels and cross sections across the shape of the valley that is a side-effect of this analysis method. This observation explains a trend observed in the precursor study, where a positive correlation between energy level and cross section was presented.[14]

Figure 11 shows an example whereby different percentage errors were added to τ_e data for a trap with $E = 0.23$ eV and $\sigma = 4 \times 10^{-15}$ cm^2; the larger the error, the broader the distribution. Fits to the E and σ within this study were subject to this effect; however, the mean fitted values for E and σ remain as expected and can therefore still be trusted. The distribution of E and σ, however, should not be trusted and is an artifact of the measurement and analysis technique. While E and σ are of scientific interest, only τ_e is required to perform CTE optimization using

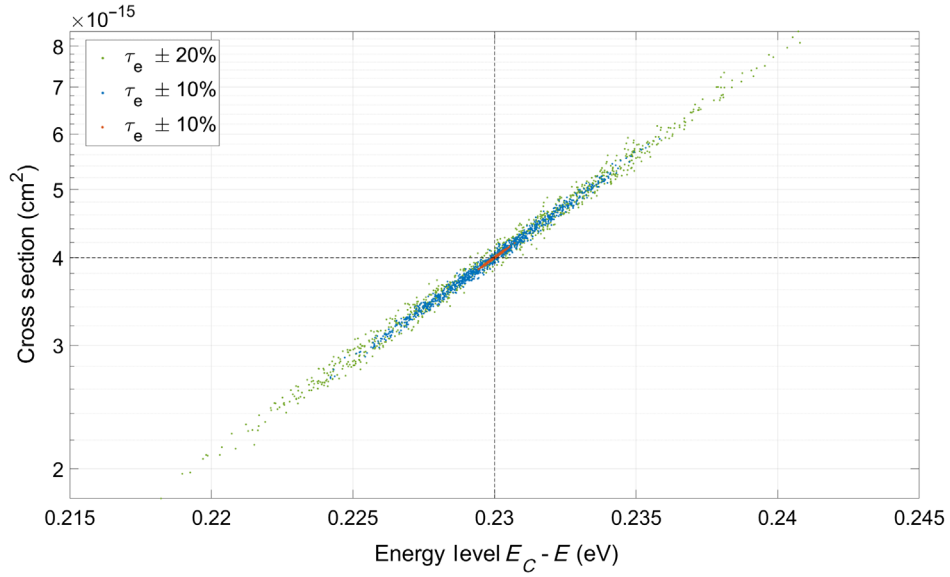

Fig. 11 Fitted values for energy and cross section for simulated τ_e data with variable percentage error for a trap with $E = 0.23$ eV and $\sigma = 4 \times 10^{-15}$ cm^2. The higher the error, the greater the spread on the distribution. The mean value for energy and cross section remained constant and correct for each case.

the trap-pumping technique. The distribution of E and σ therefore does not limit the ability to perform optimization with this data, as long as the distribution of τ_e is accurately preserved, as will later be discussed.

4 Results

4.1 *Defects within Undamaged Devices and the Control Regions of Irradiated Devices*

A small number of defects are present in as-made, undamaged EMCCDs that are remnants of wafer processing. The charge transfer performance of each control device was limited by measurement error, and so these defects do not require specific attention with respect to CTE mitigation. Nevertheless, they give an indication of impurities present that may subsequently lead to additional defects post-irradiation, and so discussion begin with the species identified in undamaged devices and the control regions of irradiated devices.

Figure 12 shows an emission time constant histogram of five devices measured at 170 K in the time parameter space of 10^{-6} to 10^{-2} s. There are four visible peaks with a consistent location but variable amplitude according to each device. The measurement was repeated at successively higher temperatures and no new peaks became visible until 240 K, where an additional peak was located at approximately 1×10^{-3} s for devices 14222-11-2 and 14222-14-2. It was later discovered this peak also contained another smaller peak, giving a total of 6 peaks. The peaks have been labeled C 1-3 and R 1-3.

A plot of defect energy level versus cross section for all defects identified within the control region of device 14222-11-2 shows the apparent correlation explained within Sec. 3 that is a result of the experimental uncertainty on the emission time constants at each temperature on the numerical fit used to extract each parameter (Fig. 13). The defects were split into groups using a 2D Gaussian mixture model that returned a mean energy level and cross section for each defect with an uncertainty that incorporated the errors in emission time constants and their effect on the observed correlation. Due to these effects, we are unable to comment in detail about the distribution of energy levels and cross sections aside from stating that the distributions presented here represent an upper limit as a result of the uncertainty on the data. The stated uncertainties

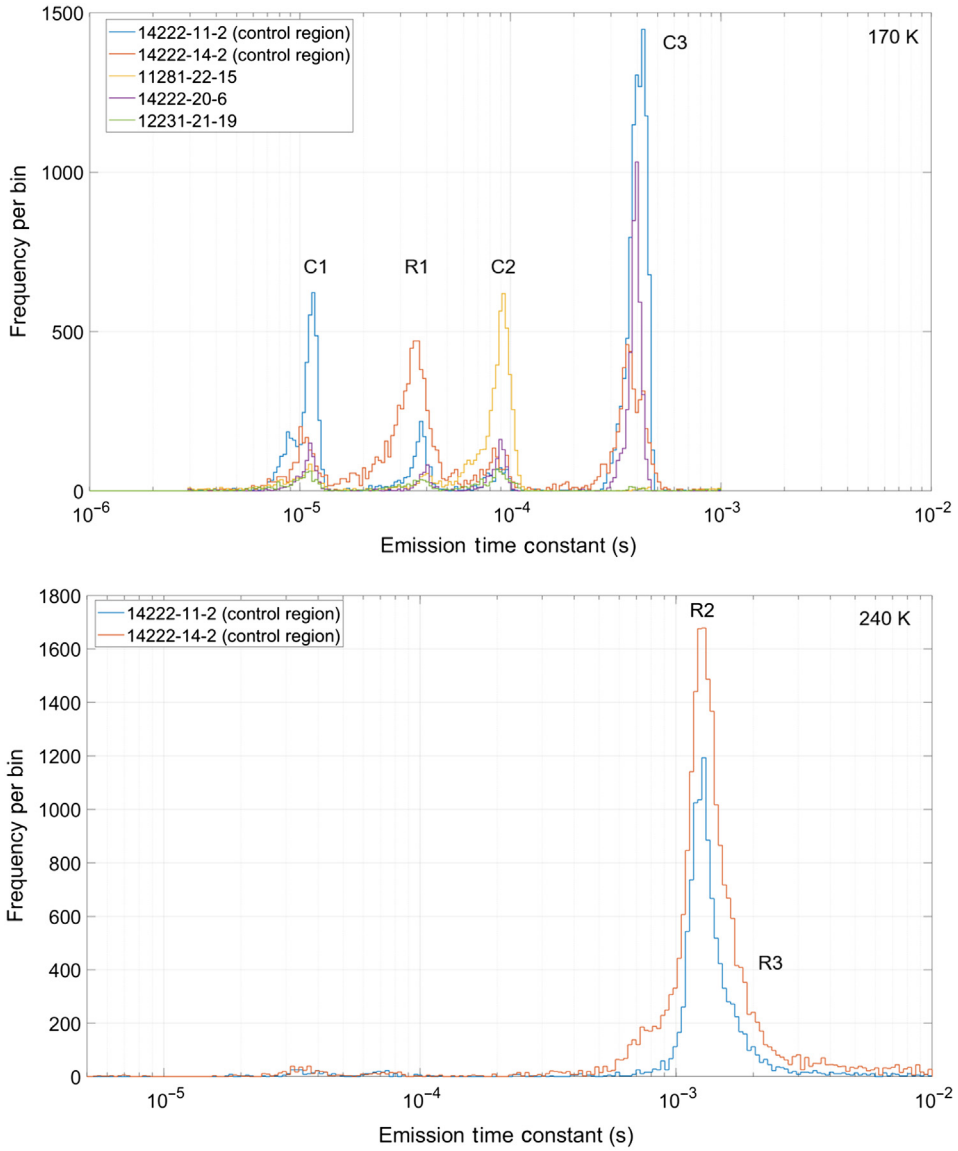

Fig. 12 Emission time constant histogram for each device obtained at 170 K (upper panel) and 240 K (lower panel) in the time parameter space of 10^{-6} to 10^{-2} s. Six defect species were identified labeled C (Control) 1 to 3, and R 1 and 3

also refer only to the error on the measured mean values for energy and cross section, as opposed to providing a limit on their distribution about the mean value. The mean energy levels and cross sections were cross referenced with other literature values to tentatively assign an atomic configuration of each defect (Table 4).

Defects C1 and C3 are believed to be due to the presence of interstitial carbon. The concentration of these defects varied between each device, which can be explained by different impurity concentrations introduced by the epitaxial growth process. The C_iP_s defects are known to be metastable and can change charge state according to the bias and illumination history of the device.[23] Each device was cooled while clocking and with steady illumination; however, it is not possible to completely exclude the possibility that the differences in observed concentrations are due to subtle differences in how each device was operated during testing.

C2 has been assigned B_iO_i since boron is known to present in these devices at a reasonably high concentration due to additional implants that define the barrier phases within the pixel. The calculated mean energy level agrees with other literature values.[20] The concentration is consistent across all devices aside from 11281-22-15.

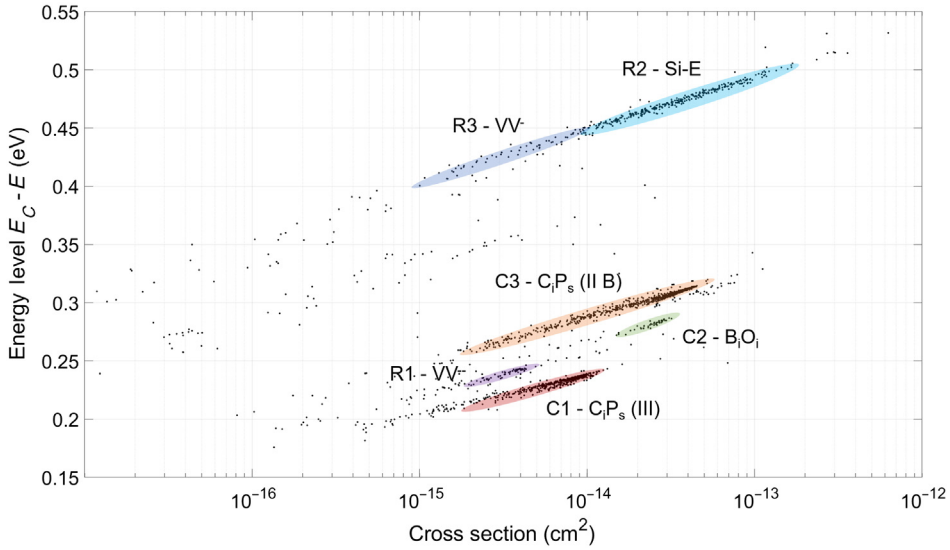

Fig. 13 Plot of energy level as a function of cross section for defects identified within the control region of device 14222-11-02. Six separate species were identified, including the silicon divacancy and Si-E center that were assumed to be a result of damage to the control region through secondary particles. The energy level and cross section exhibit a positive correlation and large spread, explained within Sec. 3. The mean values for energy level and cross section remain accurate.

Table 4 Summary of defects identified within the control region of device 14222-11-2 in the temperature range 150 to 240 K and time parameter space 10^{-6} to 10^{-2} s. Of the six defects found, three are believed to be due to intrinsic impurities within the device (C1, C2, and C3) and the other three are thought to be present due to radiation damage sustained within the shielded control regions (R1, R2, and R3).

Defect	Mean energy level (eV)	Mean cross section (cm^2)	Designation	Reference
C1	(0.23 ± 0.01)	$(6.0 \pm 2.0) \times 10^{-15}$	C_iP_s III	23
C2	(0.280 ± 0.01)	$(2.0 \pm 1.0) \times 10^{-14}$	B_iO_i	20
C3	(0.315 ± 0.01)	$(3.0 \pm 0.9) \times 10^{-14}$	C_iP_s IIB	23
R1	(0.235 ± 0.005)	$(2.6 \pm 1.2) \times 10^{-15}$	VV^{--}	14
R2	(0.475 ± 0.015)	$(3.7 \pm 0.8) \times 10^{-14}$	PV	15,16
R3	(0.42 ± 0.01)	$(2.0 \pm 1.0) \times 10^{-15}$	VV^{-}	15

R1 is in the theoretical location of the double acceptor state of the divacancy (VV^{--}) with energy level and cross section that are consistent with literature findings.[31] This is traditionally thought of as a radiation-induced defect since device processing heats the silicon beyond the thermal annealing temperature of >500 K.[41] The defect was found in a higher concentration within the control regions of devices exposed to the proton beam. Although the control regions were shielded, a small fraction of secondary particles may damage the device and create defects in this region. This phenomenon would explain the increase in R1 for device 14222-14-2 (1.45×10^{10} p/cm^2) compared to 14222-11-2 (2.09×10^9 p/cm^2).

R2 and R3 were contained within a single τ_e peak and were separated through analysis of energy levels and cross sections. Traps within the R3 peak were found to exist in the same pixel location that R1 was identified at colder temperatures. This implies they are both the same physical defect with different charge states. Based on this observation, R3 is thought to be the single acceptor state of the divacancy (VV^{-}). R2 is believed to the Si-E (PV) center.

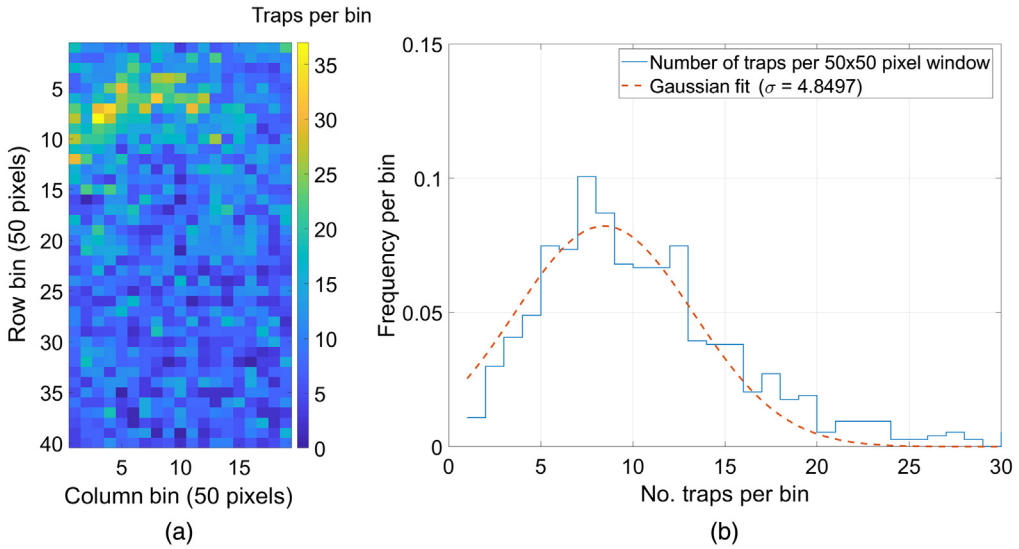

Fig. 14 (a) Number of defects identified in 50×50 pixel bins for device 11281-22-15. There is a higher local density of defects within the store region. The increase in density was found to be independent of the defect species. (b) Histogram of the number of defects found per bin.

Similar to the VV^{--}, these are also radiation-induced defects and so it appears that partial damage to the control regions has resulted in a measurable concentration. Both R2 and R3 exhibited an increase in concentration with respect to the proton fluence for the control regions of the irradiated devices, suggesting they are damage related.

The spatial distribution of defects was found to be uniform across all of the control devices tested, with the exception of device 11281-22-15 that exhibited a noticeable increase in defect density within a region of aluminum store section closest to the LS output (Fig. 14). The non-uniformity was found to be independent of the illumination (i.e., not due to an increase in background signal) and was not due to a specific trap species but a local increase in all identified species. The explanation for this observation remains unclear; the distribution is not consistent with any known processing patterns of the device and is thought to be due to a non-uniformity in the impurity concentration of the underlying epitaxial silicon. The spatial distribution of defects within windows regions 50×50 pixels in size was otherwise well represented by a Gaussian distribution (Fig. 14).

4.2 *Defects within Irradiated Devices*

Three devices in this study were irradiated using 74-MeV protons, unbiased at room temperature, to fluences of 2.09×10^9, 5.23×10^9, and 1.45×10^{10} p/cm^2 (74 MeV). These devices were shielded to maintain parallel control regions. Another device (15293-15-4) was irradiated with 5-MeV protons to a fluence of 3.65×10^9 p/cm^2. This irradiation was performed with the device biased and unshielded. (The fluence values must be scaled using the NIEL relation for an accurate comparison between each device.) Device 14222-11-2 (2.09×10^9 p/cm^2) was studied in most detail, whereas the other devices were studied in select regions of the parameter space to confirm that similar defect distributions were present and to establish the relationship between defect density and proton fluence.

The defects introduced by the irradiation far outnumbered the defects present in the undamaged devices. Figure 15 shows the spatial distribution of defects observed at 240 K for devices 14222-11-2, 14222-14-2 and at 170 K for device 15293-15-4, where the shielding pattern is clearly visible for the first two devices. Row and column profiles of defect density show an increase in density that extends beyond the shielding edge into the control region, explaining the observation of the VV^-/VV^{--} and Si-E/PV in the previous section (Fig. 16). The irradiated region also exhibits non-uniformity, with a higher density of defects at the shield boundary that decreases moving to the device edge. A possible explanation is that, during the irradiation,

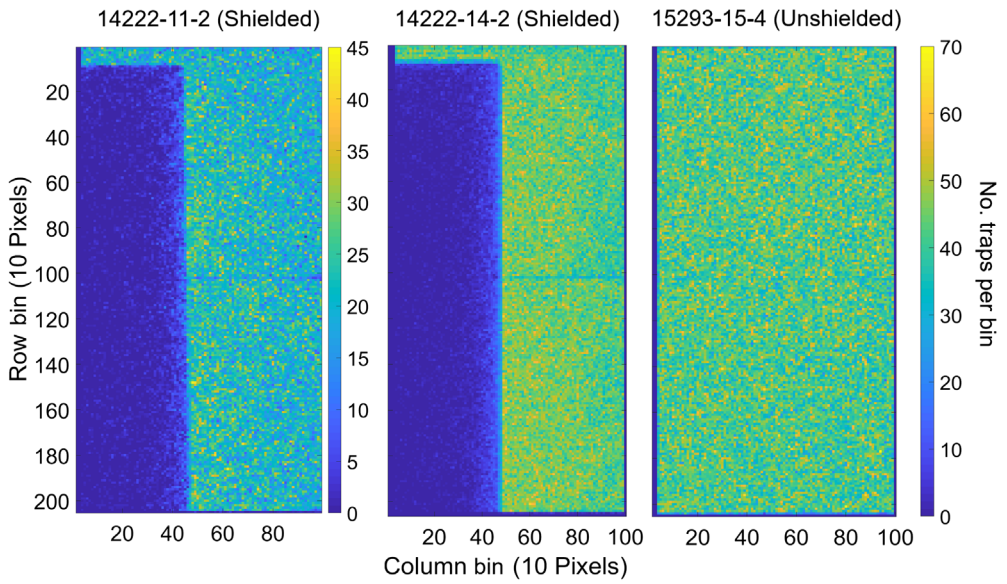

Fig. 15 Defect density distributions for three of the irradiated devices. 14222-11-2 and 14222-14-2 were shielded, whereas 15293-15-4 was unshielded. Note the orientation is such that the serial register is at the top of the image (row 0). The output node is positioned at the top left of the image (column 0).

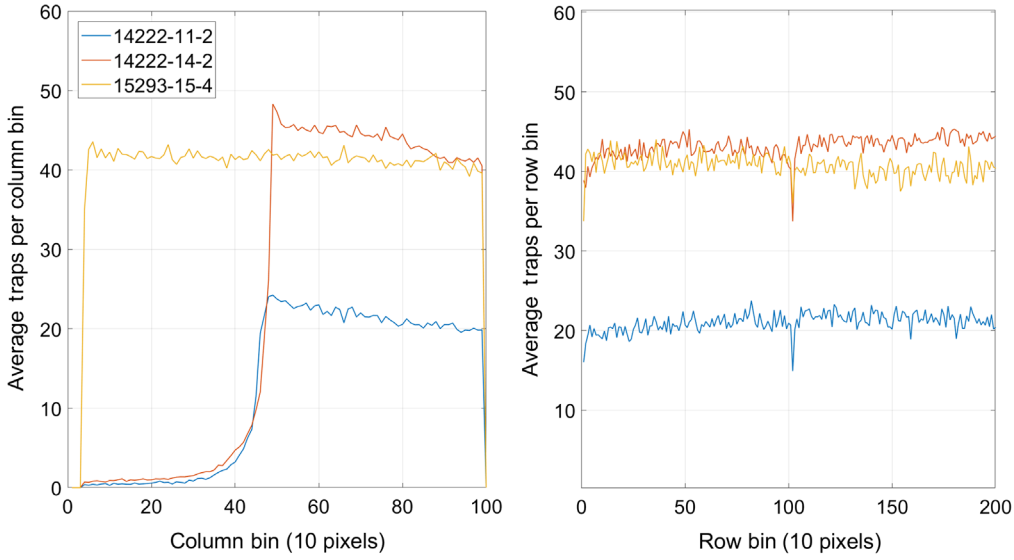

Fig. 16 Column and row profiles for the defect density distributions shown by Fig. 15. The shielded devices have an increase in density within the control region as a result of protons scattering off the shielding edge and secondary particles generated within the shielding during the irradiation. The row profiles are uniform for each device, the drop at row bin 101 is due to an illumination non-uniformity at the silicon image/store boundary generated by the trap pumping process.

primary protons scattered off the shielding edge and passed through the device with reduced energy, leading to greater damage to these regions than intended. The difference in defect density is approximately 10% across the damaged region (i.e., within ordinary limits of dosimetry); however, it is clear that the control regions are measurably affected. By comparison, the density for device 15293-15-4 (unshielded) is uniform in both the row and column directions, this result shows that applications especially sensitive to small changes in the trap density may measure performance degradation within the shielded region post-irradiation. There is a noticeable drop in the row profile for each device around row 1000; this is due to an illumination non-uniformity

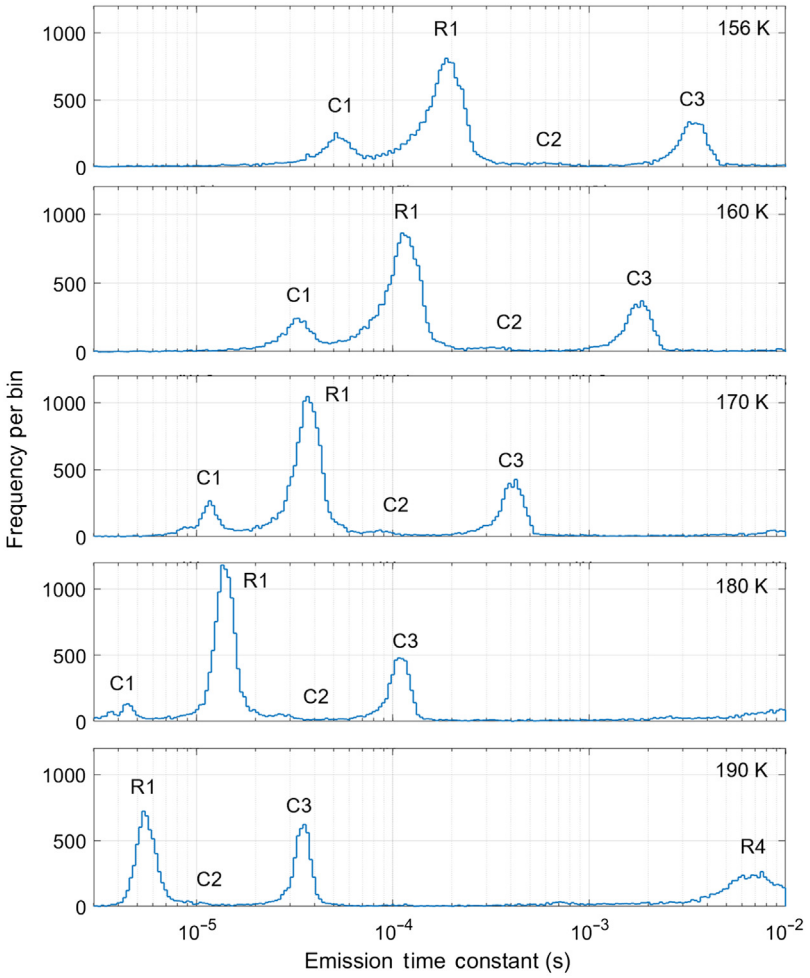

Fig. 17 Emission time constant histogram for device 14222-11-02 for temperatures ranging from 156 to 190 K, showing the presence of R1 and R4.

at the boundary between image and store sections that caused a measurable drop in the number of traps in this region for all devices.

Figures 17 and 18 show the control and irradiated regions of device 14222-11-2 in 10-K increments up to 240 K. A total of at least three new peaks are visible, with the peak at 240 K dominating the total number of radiation-induced traps by a considerable factor. An additional peak was found to be hidden within this larger peak, discovered during calculation of the energy-level and cross-section values and correlation of the location of defects at different temperatures (Figs. 19–21). Each defect has been labeled as R1 to R4. R1 is thought to be the double acceptor state of the silicon divacancy (VV^{--}) and R3 is thought to the single acceptor state (VV^{-}). Each defect exhibited an emission time constant, energy-level, and cross-section distribution consistent with the control region analysis but with much larger amplitude as a result of the irradiation. The single acceptor state was also found to be present within the same pixel location as the double acceptor state, suggesting that they were one and the same defect. R2 is thought to be the Si-E center since it has an energy level consistent with the literature expectations and is present in the highest concentration out of all defects, owing to the phosphorus-doped channel of the device.[15] R4 is a defect with yet unknown atomic configuration, and so it is referred to as the Si-U center. Analysis indicated that every pixel that contained an Si-U also contained a defect consistent with the VV^{--} (Fig. 21), indicating that the two may be related.

The Si-A center (VO_i) is often detected following irradiation of N-type epitaxial silicon.[15] The shallow energy level of approximately 0.165 eV means that the emission time constant was

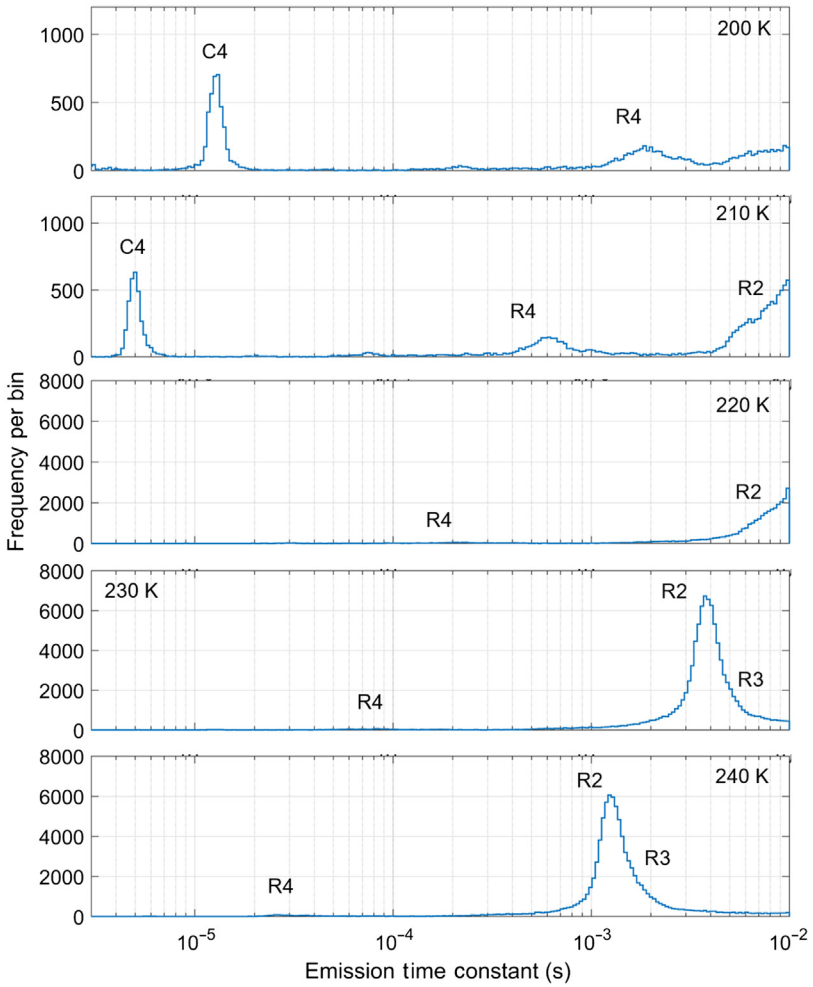

Fig. 18 Emission time constant histogram for device 14222-11-02 for temperatures ranging from 200 to 240 K, showing the presence of R2, R3 and R4. R3 is hidden within the R2 peak and was separated through additional analysis (Fig. 21).

faster than the maximum possible pumping frequency of 1 MHz for the main temperature range of interest. Modifications to the equipment lowered the minimum possible device temperature to 125 K, where an additional attempt was made to locate the Si-A.

Figure 22 shows the emission time constant histogram where there is a significant peak located at approximately 3×10^{-6} s that is consistent with previously reported energy level and cross section values.[42] The defect showed no measurable increase or difference in density attributed to irradiation. Since this defect was identified at the lowest temperature and fastest parallel clocking speeds the equipment was capable of, it is possible that what has been observed here is in fact the appearance of localized potential "pockets" that arise as a result of the experimental conditions. That being said, the results exhibited features that suggested that the dipoles were in fact due to bulk defects. The uncertainty surrounding this measurement means the result remains speculative and so literature values are quoted for energy and cross section since these remain more reliable.

A plot of the defect energy level as a function of cross section revealed the same relationship seen for the control region where there was large variance in the calculated energy levels and cross sections as a result of the analysis technique (Fig. 23). These fitted values were used to generate emission time constant histograms as a function of temperature, which were then compared to the original measured values (e.g., Figs. 17 and 18). The results were consistent, indicating that the fitted energies and cross sections accurately reproduced values for τ_e as long as the values remain coupled (i.e., the correlation was preserved). While this shows the fitted values are

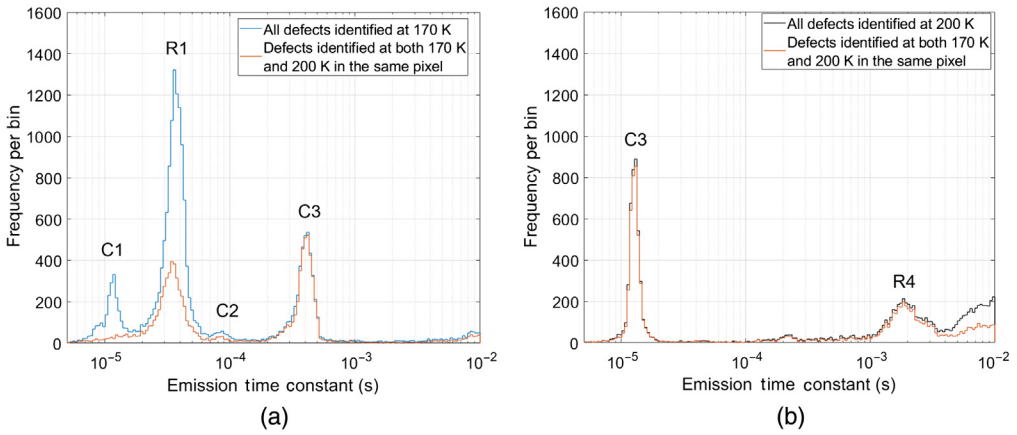

Fig. 19 Emission time constant histograms from device 14222-11-2 at 170 K and 200 K with additional analysis. (a) The original, unfiltered emission time constant histogram is shown in blue, measured at 170 K. This data was then filtered to only show traps that were also measured at 200 K with an emission time constant in the range 10^{-6} to 10^{-2} s. The C3 peak is unchanged by the filtering since it falls within the measurable range at both temperatures. C1 disappears since it cannot be measured in this time domain at 200 K. R1 decreases in amplitude, but does not disappear completely. This indicates that some fraction of R1 is also measurable at 200 K, but with a different value of τ_e than would be expected for this defect. (b) The original, unfiltered emission time constant histogram is shown in black, measured at 200 K. The 200-K data was then filtered to only show traps that were also measured at 170 K with an emission time constant in the range 10^{-6} and 10^{-2} s. The C3 peak is unchanged since it falls within the measurable range at both temperatures. R4 does not change in intensity, indicating that each R4 trap is also measured at 170 K under the R1 peak. Since R1 and R4 are observed at different temperatures under different τ_e peaks but present in the same pixel location, the suggestion is that these are different configurations of the same lattice defect.

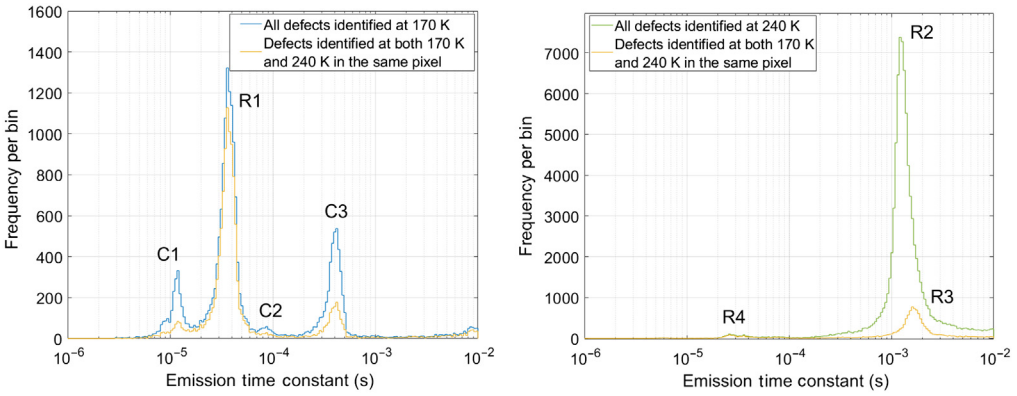

Fig. 20 The same technique implemented for Fig. 19 for measurements at 170 and 240 K. In this case, almost every pixel that contained R1 also contained a defect in the same physical location at 240 K but with a different emission time constant. At 240 K, the peak due to the Si-E–R2 is visible. The high density of the Si-E means that some pixels will contain both defects through chance alone, however simulations suggested this should account for no more than 25% of the correlation. This effect is seen for C1, C2, and C3 where a fraction was detected at both temperatures. The R3 peak at 240 K is thought to be the single acceptor state of the divacancy (VV^{-}) and showed an energy level consistent with literature expectations when the emission time constant was tracked as a function of temperature. The observation on the correlation between the Si-U and VV^{--} is interesting and unexplained. It appears that a small fraction of the VV^{--} exhibit an additional effective energy level that manifests as the Si-U as warmer temperatures.

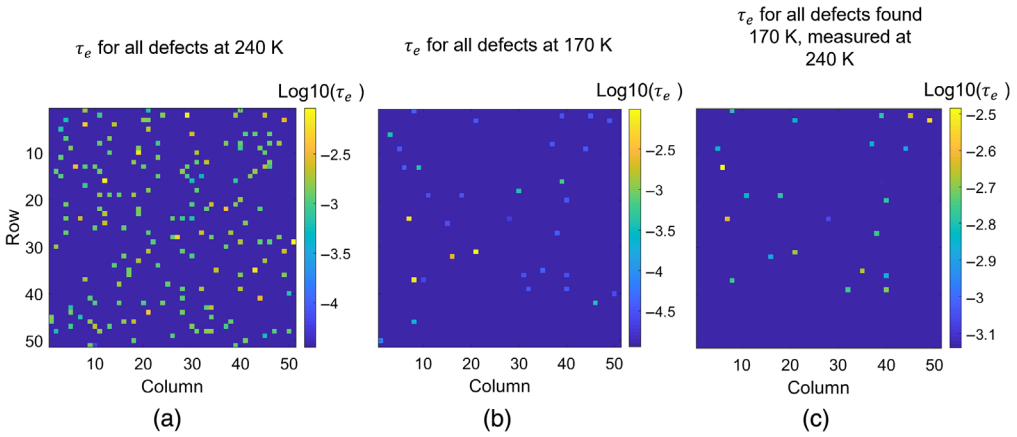

Fig. 21 50×50 pixel windows of data illustrated by Fig. 20. (a) Emission time constant and location for all defects located at 240 K, this includes data for R2, R3, and R4. (b) Emission time constant and location for all defects identified at 170 K, this includes C1, C2, C3, and R1. The 240-K data were then filtered to only include information for defects identified at both 240 and 170 K in the same pixel location. The result is shown in (c), where only data for R3 is displayed. Comparison of (b) and (c) shows that the defects are present in the same pixel location but with different τ_e, due to the different charge state of the VV probed at each temperature.

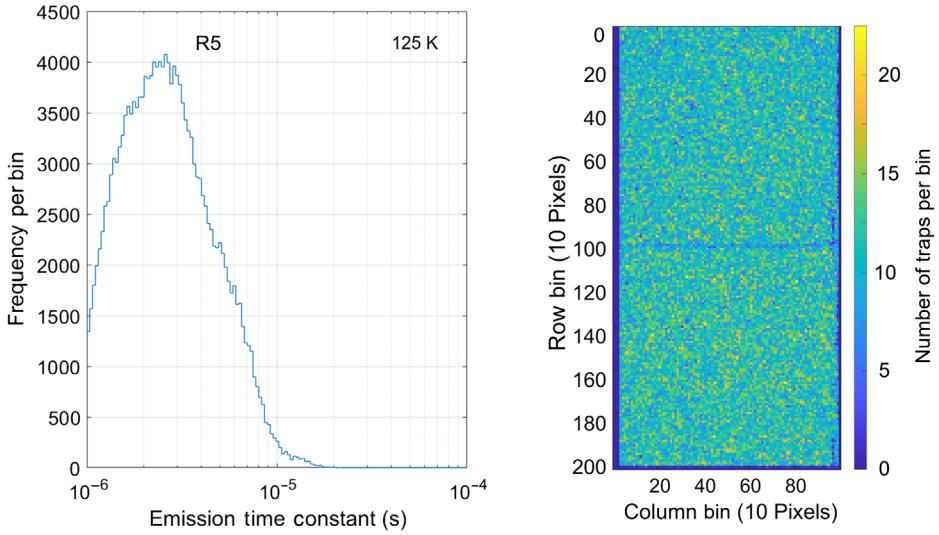

Fig. 22 Emission time constant obtained for device 14222-11-02 at 125 K, highlighting the presence of a defect believed to be the Si-A center. The right panel shows the spatial distribution of the defect across the device. No measurable increase or difference in density could be attributed to the irradiation. This defect was identified at both the coldest temperature the equipment was capable of, and the fastest parallel clocking speeds. It is possible that what has been observed here is in fact the appearance of localized potential "pockets" that arise as a result of the experimental conditions. That being said, the results exhibited features that suggested that the dipoles were in fact due to bulk defects.

reliable, it is less than useful for future optimization and correction algorithms since it means that the emission cross sections and energy levels are specific to this dataset. To account for this, the mean energy levels and cross sections from this data were used in combination with a cross-section distribution that would accurately reproduce the distribution in τ_e as a function of temperature:

$$\tau_e = \frac{1}{\sigma_{\text{dist}} N_C v_{\text{th}}} e^{\frac{E}{k_B T}}, \tag{6}$$

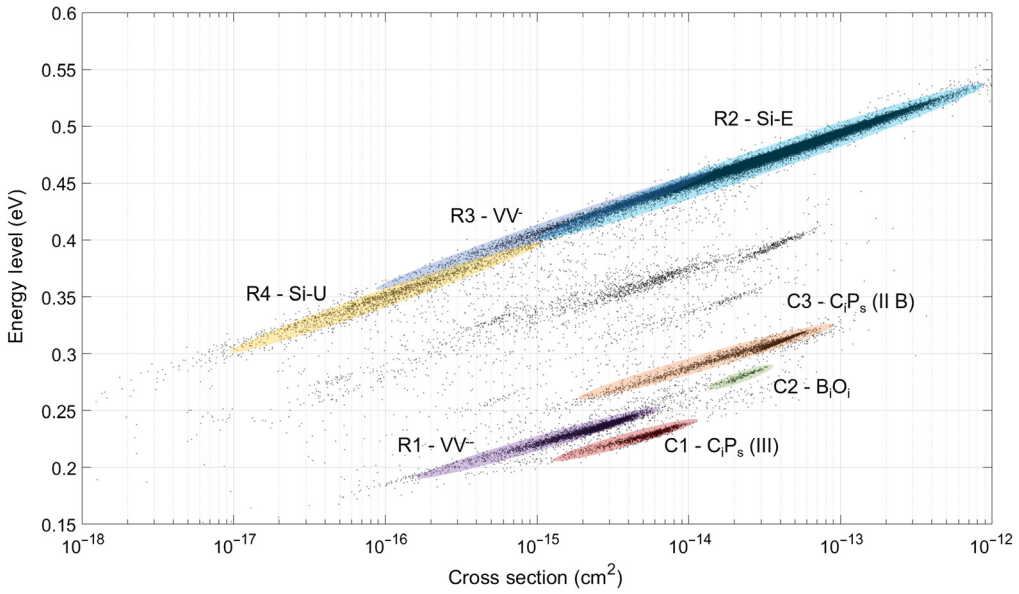

Fig. 23 Plot of energy level as a function of cross section for defects identified within the irradiated region of device 14222-11-02. A total of seven species are labeled, four of which are believed to be due to irradiation. The Si-A center is believed to be present but was not probed by these measurements. The energy level and cross section exhibit a positive correlation and large spread, explained within Sec. 3. The mean values for energy level and cross section remain accurate.

Table 5 Summary of defects identified within the irradiated region of device 14222-11-2 in the temperature range 150 to 240 K and time parameter space 10^{-6} to 10^{-2} s, with an additional measurement at 125 K confirming that the literature values for the Si-A center seemed sensible.

Defect	Mean energy level (eV)	Mean emission cross section σ_μ (cm^2)	Fitted cross section variance (c)	Designation	Reference
R1	(0.235 ± 0.005)	$(2.6 \pm 0.5) \times 10^{-15}$	$(4.0 \pm 0.5) \times 10^{-16}$	VV^-	14, 15
R2	(0.475 ± 0.015)	$(3.7 \pm 0.8) \times 10^{-14}$	$(5.9 \pm 0.7) \times 10^{-15}$	PV	15, 16
R3	(0.42 ± 0.01)	$(2.0 \pm 1.0) \times 10^{-15}$	$(5.0 \pm 0.6) \times 10^{-16}$	VV^-	15
R4	(0.37 ± 0.01)	$(8.7 \pm 0.7) \times 10^{-15}$	$(3.0 \pm 0.5) \times 10^{-15}$	Si-U	24
R5	0.165	6.1×10^{-15}	$(1.6 \pm 0.8) \times 10^{-14}$	$VO_i^{(-/0)}$	15, 16, 18

$$\sigma_{\text{dist}}(x) = e^{-\frac{(x-\sigma_\mu)^2}{2c^2}}, \tag{7}$$

where σ_{dist} refers to the distribution in cross-section values (assumed Gaussian), σ_μ is the mean cross-section value, and c is a measure of the variance of the distribution; a free parameter that is fitted for each trap. This approximation to the defect distribution allows accurate reproduction of τ_e without the need for the individual fitted energy-level and cross-section values from each dataset. The fitted values of σ_{dist} are presented in Table 5.

Figure 24 shows a plot of the emission time constant of each defect as a function of temperature, reproducing the form of Fig. 5 but with experimental data from 14222-11-2. The data have been binned to give an impression of the relative densities of each defect. It is clear that, within the parameter space probed, the VV^{--} and the Si-E are the dominant defects that form following the irradiation. The Si-U appears but at a density that is comparable or lower than then some of the defects present in undamaged devices. The distribution of the Si-U differs from the other defects in that it is a broad peak that spans a comparatively large time domain compared to the other defects. This was reflected in a large value of σ_{dist} relative to σ_μ when compared to the other defects (Table 5). While there are clearly dominant traps, there is also a distribution of defects

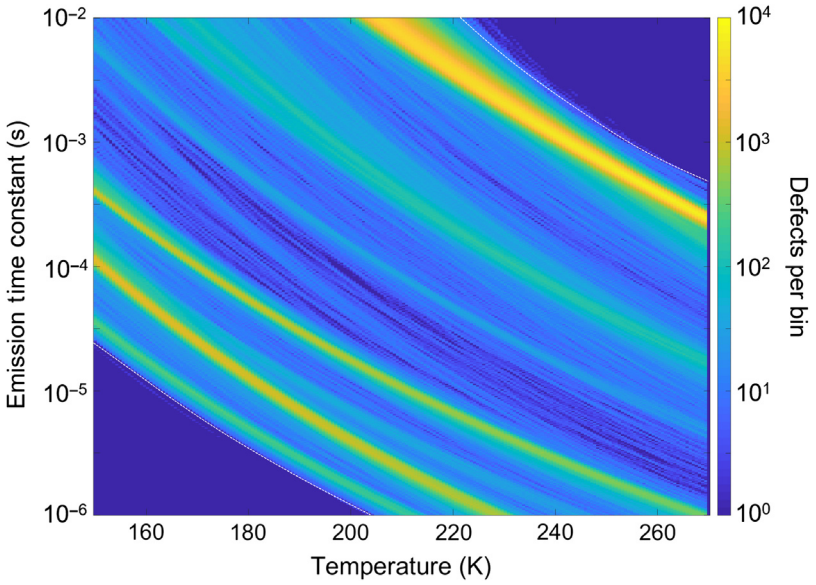

Fig. 24 Plot of emission time constant versus temperature for all defects identified in the irradiated region of device 14222-11-02. For this plot, emission time constant bins were logarithmically spaced between 10^{-6} and 10^{-2} with 200 points. The temperature bin spacing was 0.1 K. The temperature data were obtained with a wider 2-K spacing, and so the values for E and σ were used to calculate intermediate values. Data are valid between the boundaries of the white dashed lines.

between the dominant species that were not explicitly identified in this study. There is a cluster of defects with mean energy $E = E_C - 0.39$ eV and $\sigma_\mu = 3 \times 10^{-14}$ cm^{-2} that could potentially be the acceptor state of the self-interstitial oxygen interstitial ($Si_iO_i^-$), and an additional cluster with mean energy $E = E_C - 0.37$ eV and $\sigma_\mu = 7 \times 10^{15}$ cm^{-2} that could be due to the C_iP_s complex (Fig. 23, Table 1). The number density of these defects was low (between 100× and 1000× less than the Si-E center), and they could not attributed to any peaks within the emission time constant data. Larger format devices may have these defects present in sufficient number for peaks to be visible; however for the devices in this study, these defects were too few in number for accurate identification and so these designations remain speculative.

4.3 *Calculating Defect Densities*

The results presented in Sec. 4.2 allow accurate reproduction of the emission time constant distributions of each of the primary defects as a function of temperature; however, they give no representation of the relative abundance of each species. This is the final piece of information required in order to use the information for CTI estimation, optimization, and correction.

The trap-pumping technique gives a number density, in units of traps per pixel, that can be converted into a density value (defects $\cdot\ \mu$m^{-3}) through calculation of the volume of silicon probed the charge packet during the trap-pumping process. The analysis was performed on scheme 1 for the CCD201, although in principle the same technique can be used on any scheme or device. The volume of the charge packet is difficult to define in conventional terms since there is no fixed boundary, but rather a decreasing region of signal density that surrounds a core with a maximum value equivalent to the peak doping density of the device ($\approx 10^{16}$ cm^{-3} for a CCD). Instead, it is more appropriate to define an "effective volume" available for capture since it is only when charge is captured that it will be seen in the trap-pumping process. The capture probability is described by a capture time constant, τ_C, and the probability of capture (P_C) is then given by the combination of the time constant and the total time the charge spends in the vicinity of the trap (t_{dw})

$$\tau_C = \frac{1}{\sigma_n n_E v_{\text{th}}}, \tag{8}$$

Table 6 The estimated volume of silicon probed by the trap pumping technique for a 10,000 e^- signal packet for a given temperature, capture cross section, and dwell time. These values were used to calculate the cutoff density, ρ_{cut}, that was in turn used to define the volume of the cloud probed using pumping scheme 1 in TCAD.

Defect species	Temperature (K)	$\sigma_n(\text{cm}^2)$	t_{dw} (s)	n_E (e^-/cm^3)	Volume probed (μm^3) (10,000 e^- scheme 1)
VV^{--}	170	1.2×10^{-15}	1×10^{-4}	7.10×10^{11}	7.8
Si-U	210	1.4×10^{-15}	1×10^{-4}	5.30×10^{10}	8.9
PV (Si-E)	240	3.7×10^{-15}	1×10^{-3}	1.87×10^{10}	9.4
VV^-	240	1.6×10^{-15}	1×10^{-3}	4.30×10^{10}	9.0
VO_i (Si-A)	125	6.2×10^{-15}	5×10^{-6}	3.00×10^{12}	7.0

$$P_C = 1 - e^{-\frac{t_{dw}}{\tau_C}}, \tag{9}$$

where n_e is the signal density, v_{th} is the thermal velocity of the electron, and σ_n is the capture cross section of the trap (note this differs from the emission cross section). The capture cross section cannot easily be measured through the trap-pumping technique; however for the defects of interest to CCDs, past studies have estimated values of order 10^{-15} to 10^{-14} cm^2.[16] The capture probability is an output of the analysis [Eqs. (3)–(5)] and so it is possible to filter the data in such a way that the number of traps with an average capture probability greater than, e.g., 0.8, are selected. For a pumping scheme, t_{dw} is equivalent to t_{ph} and so it is possible to rearrange Eqs. (8) and (9) in such a way as to calculate a value of n_E that is used to define the effective edge of the charge packet relevant to capture. This value is termed the cutoff density, ρ_{cut}. For the example of the silicon divacancy (VV^{--}) probed at 170 K, with $P_C \geq 0.8$, $\rho_{\text{cut}} \approx 10^{10}$ e^-/cm^3. This method was used to define the edge of the charge packet in TCAD for each of the main trap species introduced by the irradiation (Table 6). This method is prone to uncertainty; in practice t_{ph} is not fixed but varied over the range of 10^{-6} and 10^{-2} s and so the value chosen was equal to the peak of the emission time constant histogram measured at a given temperature. The capture cross sections are also poorly defined and are expected to vary by up to an order of magnitude.

This method for estimating density should in principle be valid for any signal size used for pumping. Figure 25 shows the number of VV^{--} identified with $P_C \geq 0.8$ for signal sizes ranging from 10,000 e^- to 20,000 e^-. Both the number of traps and predicted volume probed by pumping increase, but by slightly different factors. Doubling the signal size from 10,000 e^- represents a predicted increase in volume of ×1.4, whereas the increase in detected traps is slightly lower at ×1.25. The discrepancy is believed to be due to the change in signal size throughout the pumping process. For the example of Scheme 1 with 10,000 pumps, the signal size will decrease by as much as 2500e^- in the presence of a trap with $P_c = 1$; a 14% decrease in volume according to TCAD. Future iterations of this method can reduce this effect by limiting the number of pumps to, e.g., 1000, and improving data quality by averaging frames to reduce the impact of shot noise on trap detection.

An additional estimate for the volume of the charge packet is also possible through the knowledge of the pixel dimensions and the charge handling capacity. The CCD201 has a measured full well capacity of approximately 80,000 e^-. The pixels are 13-μm square with 3-μm channel stops, leaving 9 μm for charge storage. Within the pixel, charge is stored beneath the storage phases that are each 4.5 μm in length. The buried channel is located approximately 0.5 μm into the substrate.[11] This gives a storage volume of approximately 20 μm per storage phase. It is worth noting this calculation has ignored the effects of fringing fields that reduce the volume further. For large signal levels, the volume occupied by a charge packet has been shown to be proportional to the square root of the signal size. A reduction in signal size from 80,000e^- down to the 10,000 e^- used for pumping therefore constitutes an approximate factor 3 reduction in volume. The pumping scheme probes both storage phases, meaning that we can expect a 10,000 e^- signal packet to probe approximately $(20\times2)/3 \approx 13$ μm^3 of silicon as an

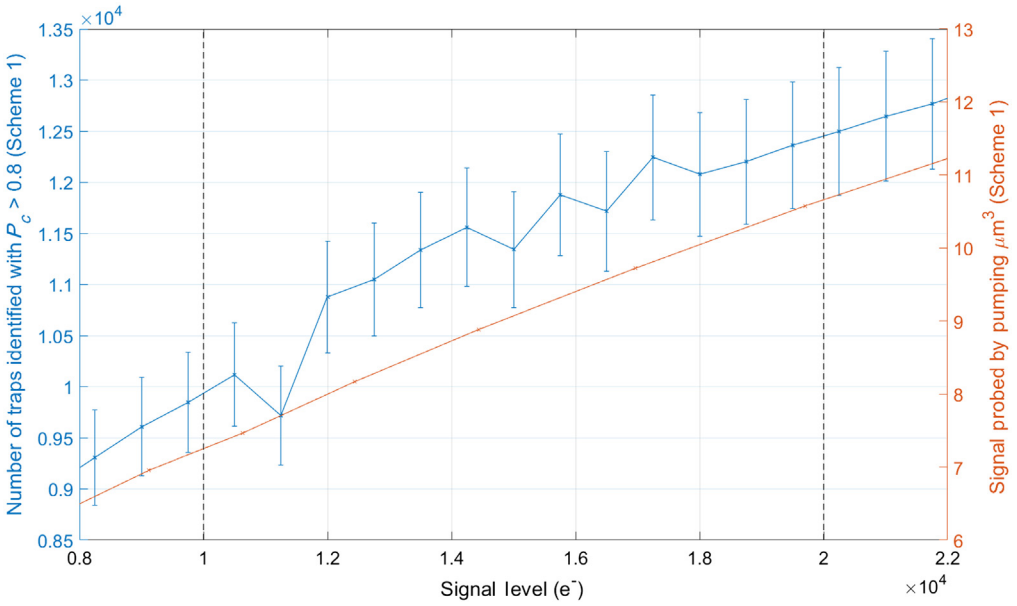

Fig. 25 Signal probed by pumping (Scheme 1) versus the number of traps identified with $P_c > 0.8$ for various signal sizes. The experimental data were obtained using device 14222-11-2 at 170 K, with the VV^{--} as the trap of interest. The TCAD data were obtained using a 3D CCD201-20 pixel simulated at the same bias conditions as used for pumping scheme 1. The cutoff density was chosen to as 7.10×10^{11} e^-/cm^3 (Table 6).

upper limit. This is close to the TCAD estimated values, and so we believe our estimates of defect density to be accurate within a factor of ×2.

Table 7 contains a summary of defect density as a function of proton fluence for each of the irradiated devices in this study. The highest density was attributed to the Si-A center. There is a large degree of uncertainty surrounding the data for this defect in particular, however we note

Table 7 Summary of density calculations for each of the defects and devices studied. Results were obtained as a function of proton fluence for the VV^{--}, Si-E, and Si-U. For the VV^-, only a single calculation was performed due to the difficultly in isolating it from the peak of the Si-E center. The calculation suggested that results at higher fluences would be unreliable as the density of the Si-E continued to increase. The Si-A was thought to be found on device 14222-11-2 (Fig. 22), however showed no noticeable increase with fluence. The number found is presented since this is the best data available, however it should be treated with uncertainty. The number found relates to a charge packet of 10,000 e^- used with Scheme 1 in a pixel region of interest 2000 pixels × 500 pixels in size. For the Si-E center at the highest fluence, the density of the defect was approaching 1 trap per 2 pixels (the upper limit) and so data from Schemes 3 and 4 were also used to verify the value since they probe a smaller fraction of the pixel area.

	Proton fluence (74 MeV)					
	$(2.09 \pm 0.2) \times 10^9$		$(5.23 \pm 0.52) \times 10^9$		$(1.45 \pm 0.15) \times 10^{10}$	
Defect	Number found	Density (μm^{-3})	Number found	Density (μm^{-3})	Number found	Density (μm^{-3})
VV^{--}	7358	9.43×10^{-4}	24074	3.10×10^{-3}	47506	6.10×10^{-3}
Si-E	67820	6.40×10^{-3}	141692	1.25×10^{-2}	364991	3.38×10^{-2}
Si-U	2242	2.49×10^{-4}	5938	6.60×10^{-4}	13553	1.50×10^{-3}
VV^-	7018	7.80×10^{-4}	—	—	—	—
Si-A	83250	1.20×10^{-2}	—	—	—	—

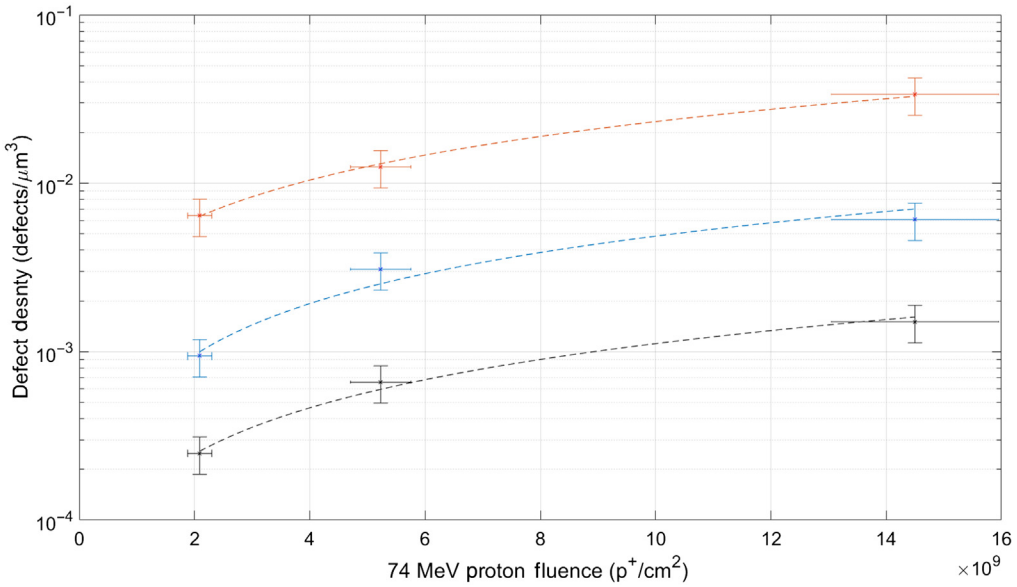

Fig. 26 Plot of defect density versus proton fluence for the devices irradiated with 74-MeV protons. A logarithmic scale was used so all values were clearly visible, the dashed lines are linear fits to the data.

that other studies have also presented a density that is approximately equal to 2× that of the Si-E.[11,43] Each state of the VV showed a similar density. This was expected and is also an artifact of the measurement technique. The separation of the VV^{--} from the Si-E center peak meant that the same pixel also had to exhibit a VV^{--}, so in practice the density value for this defect had this value as an upper limit. Any VV^{-} that were not detected would have been incorporated into the value for the Si-E. The Si-U has the lowest density, approximately 3× less than the VV^{--}. A plot of each defect density as a function of fluence showed a linear dependence on proton fluence for the fluence levels of this study (Fig. 26).

5 Summary and Conclusions

This study has identified a total of 8 unique silicon defects within irradiated and unirradiated CCD201 EMCCDs. The mean energy levels and cross sections have been presented alongside density values for the dominant defects that can influence CTE. A means to replicate the spread in emission time constants has also been presented in the form of a Gaussian distribution about the mean value. When combined, this information allows replication of the defect distributions observed in this study for any temperature in the range 150 to 240 K. Figure 27 shows the example of a measured emission time constant histogram at both 170 and 240 K. In each panel, the raw data are shown alongside the distributions recreated from fitted energy levels and cross sections, and a randomly generated distribution that used the cross-section distribution function for the VV^{--} (Table 5). At 170 K, the agreement between each of the three datasets is excellent for the VV^{--}. At 240 K, there is a discrepancy in the number and the shape of the distribution for the Si-E center and VV^{-}. The energy levels and cross sections are reliant on a good quality fit to the emission time constant as a function of temperature, and at the warmer temperatures dark current, hot pixels and a high defect density interfered with data quality. A number of Si-E candidates were therefore discarded during the fit process, leading to a reduction in the reconstructed number. Either side of the peak is also an extended tail that is partially reconstructed using the fitted energy levels and cross sections, but not reconstructed using the σ_{dist} formalism. It is unclear whether this is a feature of the lattice defect distribution, or just due to a tail of poor-quality data that have skewed a fraction of the measured values for τ_e. Comparison of measured CTI data compared to the simulated and measured trap distributions is the important next step to verify whether additional measurements are required to better replicate the emission time constant distribution of this defect.

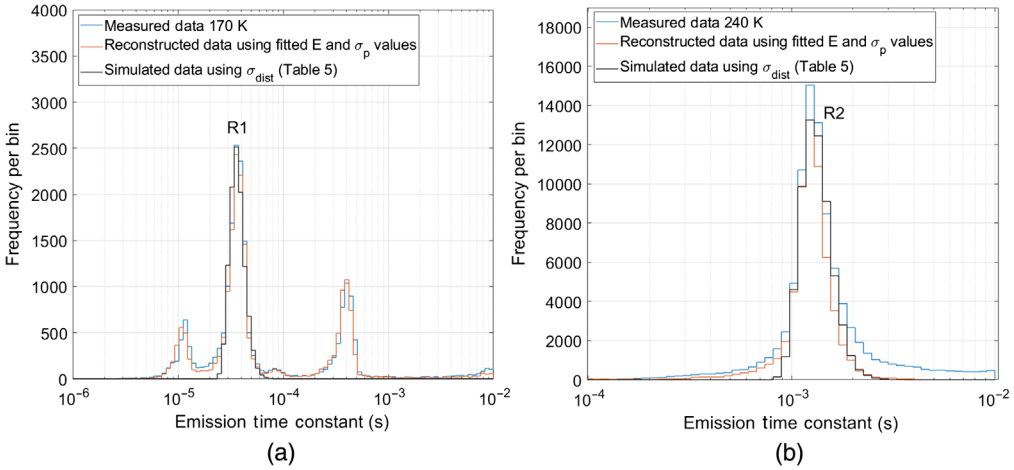

Fig. 27 Emission time constant histograms at (a) 170 and (b) 240 K showing a comparison between raw measured data, reconstructed data using fitted values for energy level and cross section, and the simulated distribution using the cross section parameters in Table 5.

Many observations made in this investigation open the door to interesting further study. The identification of the Si-A remains speculative and requires additional data at lower temperatures. The technique used to calculate the defect densities was reliant on TCAD simulations of the CCD201 image pixel and measurements of the VV^{--} as a function of signal size. The volumes returned by TCAD are believed to be fairly accurate; however, the measurements of the VV^{--} density as a function of signal size were limited by the change in signal size throughout the pumping process. Further measurements with a reduced number of pumping cycles should yield more accurate results to match the TCAD expectations. Despite these improvements, the values presented here are a useful step toward CTE optimization on these devices. For example, a useful feature of the energy-levels and cross-section distributions presented here is that they allow the inference of the emission time constant distribution of all traps at different CCD operating temperatures. Figure 28 shows an emission time constant histogram for device 14222-11-02 at

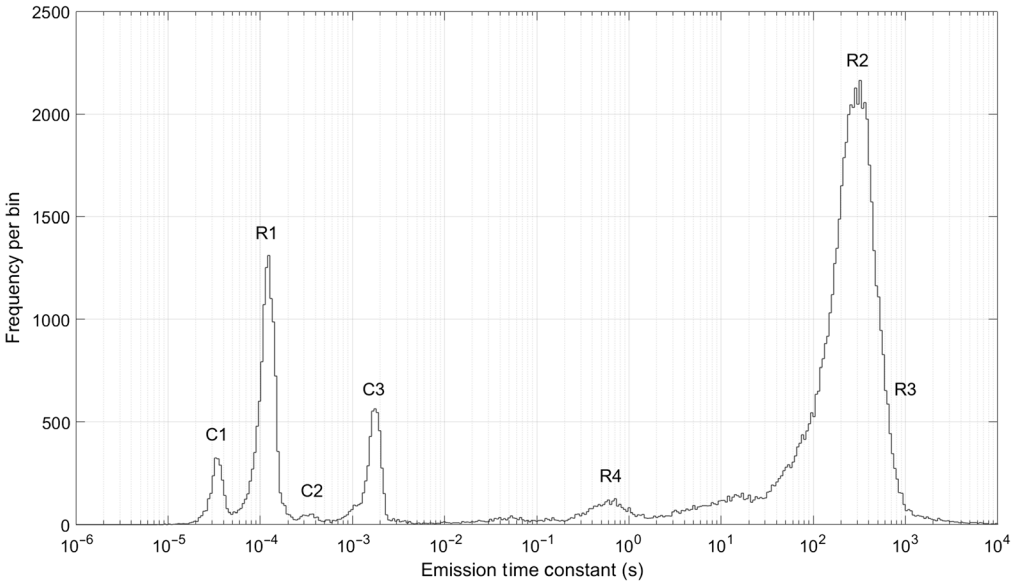

Fig. 28 Emission time constant histogram of all traps identified in device 14222-11-2 at 170 K. While the Si-U, Si-E, and VV^{-} were not explicitly measured at this temperature using trap pumping, the energy levels and cross sections of these defects measures at warmer temperatures were used to infer the expected value at colder temperatures.

160 K showing all identified defects. The Si-U and Si-E peaks extend from the 10^{-1} to 10^{3} s range; a region that cannot currently be probed by trap pumping, yet remains relevant to CTI mitigation. A future study shall aim to use this information to optimize charge transfer efficiency on the same irradiated CCD201s through minimization of the number of effective traps during the readout process. It is hoped that this technique shall demonstrate the utility of the data provided by this study for future applications that can benefit from improved charge transfer performance in the presence of proton damage.

6 Appendix

In this study, the formalism used to describe defect energy levels and cross sections is based upon Shockley–Read–Hall statistics that are well described within[16] and the associated references. All equations and constants used are described below, with additional references as needed:

The emission time constant of the trap is given by

$$\tau_e = \frac{1}{\sigma_p N_C v_{\text{th}}} e^{\frac{E}{k_B T}},$$

where σ_p is the capture cross section for holes, v_{th} is the thermal velocity of the electron, and N_C is the effective density of states within the conduction band.

The thermal velocity is given by[44]

$$v_{\text{th}} = \sqrt{\frac{3k_B T}{m^*_{dC}}}.$$

N_C is given by

$$N_C = 2\left(\frac{2\,\pi m^*_{dc} k_B T}{h^2}\right)^{\frac{3}{2}},$$

where m^*_{dc} denotes the density of state effective electron mass in the conduction band. Silicon has six conduction-band minima that form ellipsoidal surfaces of constant energy. The effective mass is given by[45]

$$m^*_{dC} = 6^{\frac{2}{3}}(m^{*2}_t m^*_l)^{1/3},$$

where m^*_t and m^*_t are the transverse and longitudinal effective masses associated with the constant energy surfaces, respectively:

$$\frac{m^*_t}{m_0} = 0.1905 \times \frac{E_g(0)}{E_g(T)},$$

$$\frac{m^*_l}{m_0} = 0.1963,$$

where m_0 is the reset mass of the electron, $E_g(0) = 1.1692$ eV and, from Ref. 46

$$E_g(T) = E_g(0) - \frac{\alpha_g T^2}{T + \beta_g}.$$

$$\alpha_g = 4.9 \times 10^{-4}\ \text{eV/K},$$

$$\beta_g = 655\ \text{K}.$$

The remaining symbols take their usual meaning and values; h is the Planck's constant and k_B is the Boltzmann constant. It is noteworthy that the units of k_B vary according to usage in each of these equations.

References

1. P. Jerram et al., "The LLCCD: low-light imaging without the need for an intensifier," *Proc. SPIE* **4306**, 178–186 (2001).
2. C. Mackay et al., "High-speed, photon-counting CCD cameras for astronomy," *Proc. SPIE* **7742**, 774202 (2010).
3. O. Daigle et al., "Extreme faint flux imaging with an EMCCD," *Publ. Astron. Soc. Pac.* **121**, 866 (2009).
4. L. K. Harding et al., "Technology advancement of the CCD201-20 EMCCD for the WFIRST coronagraph instrument: sensor characterization and radiation damage," *J. Astron. Telesc. Instrum. Syst.* **2**, 011007 (2015).
5. R. M. Morgan et al., "Technology maturity update for the Habitable-Zone Exoplanet Imaging Observatory (HabEx) concept," *Proc. SPIE* **11115**, 111150N (2019).
6. M. R. Bolcar et al., "Initial technology assessment for the Large-Aperture UV-Optical-Infrared (LUVOIR) mission concept study," *Proc. SPIE* **9904**, 99040J (2016).
7. R. Kohley et al., "The radiation environment at L2 as seen by Gaia," *Proc. SPIE* **9154**, 915406 (2014).
8. J. R. Srour, C. J. Marshall, and P. W. Marshall, "Review of displacement damage effects in silicon devices," *IEEE Trans. Nucl. Sci.* **50**, 653–670 (2003).
9. V. A. J. Van Lint et al., *Mechanisms of Radiation Effects in Electronic Materials*, Vol. **1**, p. 370, Wiley-Interscience, New York (1980).
10. A. S. Grove, Physics and Technology of Semiconductor Devices, Vol. **180**, John Wiley and Sons, Inc., New York (1967).
11. A. D. Holland, "The effect of bulk traps in proton irradiated EEV CCDs," *Nucl. Inst. Methods Phys. Res. A* **326**, 335–343 (1993).
12. J. H. Tutt et al., "The noise performance of electron-multiplying charge-coupled devices at soft x-ray energy values," *IEEE Trans. Electron Devices* **59**, 2192–2198 (2012).
13. D. R. Smith et al., "EMCCDs for space applications," *Proc. SPIE* **6276**, 62760K (2006).
14. N. Bush et al., "Development of *in-situ* trap characterisation techniques for EMCCDs," *J. Instrum.* **13**, C02025 (2018).
15. A. Hallén et al., "Lifetime in proton irradiated silicon," *J. Appl. Phys.* **79**, 3906 (1996).
16. M. Moll, "Radiation damage in silicon detectors," *Nucl. Instrum. Methods Phys. Res.* **123**(3), 615–618 (1984).
17. K. A. Abdullin, B. N. Mukashev, and Y. V. Gorelkinskii, "Metastable oxygen-silicon interstitial complex in crystalline silicon," *Semicond. Sci. Technol.* **11**, 1696–1703 (1996).
18. D. J. Hall et al., "Determination of *in situ* trap properties in CCDs using a 'single-trap pumping' technique," *IEEE Trans. Nucl. Sci.* **61**, 1826–1833 (2014).
19. G. D. Watkins and J. R. Troxell, "Negative-U properties for point defects in silicon," *Phys. Rev. Lett.* **44**, 593 (1980).
20. J. Schmidt, C. Berge, and A. G. Aberle, "Injection level dependence of the defect-related carrier lifetime in light-degraded boron-doped Czochralski silicon," *Appl. Phys. Lett.* **73**, 2167 (1998).
21. S. D. Brotherton and P. Bradley, "Defect production and lifetime control in electron and γ-irradiated silicon," *J. Appl. Phys.* **53**, 5720–5732 (1982).
22. L. W. Song et al., "Bistable interstitial-carbon substitutional-carbon pair in silicon," *Phys. Rev. B* **42**, 5765–5783 (1990).
23. E. Gürer, B. W. Benson, and G. D. Watkins, "Configurational metastability of carbon-phosphorus pair defects in silicon," *Mater. Sci. Forum* **83–87**, 339–344 (1992).
24. N. L. Bush, "The impact of radiation damage on electron multiplying CCD technology for the WFIRST coronagraph," PhD Thesis, The Open University (2018).
25. R. N. Hall, "Electron–hole recombination in germanium," *Phys. Rev.* **87**(2), 387 (1952).
26. W. Shockley and W. T. Read, "Statistics of the recombinations of holes and electrons," *Phys. Rev.* **87**, 835 (1952).
27. B. G. Magorrian and N. M. Allinson, "Soft x-ray damage in CCD detectors," *Nucl. Inst. Methods Phys. Res. A* **273**, 599–604 (1988).
28. A. Short et al., "An analytical model of radiation-induced charge transfer inefficiency for CCD detectors," *Mon. Not. R. Astron. Soc.* **430**, 3078–3085 (2013).

29. D. J. Hall et al., "Modelling charge transfer in a radiation damaged charge coupled device for Euclid," *Proc. SPIE* **8453**, 845315 (2012).
30. R. Massey et al., "An improved model of charge transfer inefficiency and correction algorithm for the Hubble Space Telescope," *Mon. Not. R. Astron. Soc.* **439**, 887–907 (2014).
31. D. Wood et al., "A study of the double-acceptor level of the silicon divacancy in a proton irradiated n-channel CCD," *Proc. SPIE* **9915**, 99150J (2016).
32. N. J. Murray et al., "The relationship between pumped traps and signal loss in buried channel CCDs," *Proc. SPIE* **8860**, 88600H (2013).
33. D. Wood et al., "Evolution and impact of defects in a p-channel CCD after cryogenic proton-irradiation," *IEEE Trans. Nucl. Sci.* **64**, 2814–2821 (2017).
34. I. V. Kotov, P. O'Connor, and N. Murray, "Pocket pumped image analysis," *Proc. SPIE* **9154**, 91541K (2014).
35. N. J. Murray et al., "Mitigating radiation-induced charge transfer inefficiency in full-frame CCD applications by 'pumping' traps," *Proc. SPIE* **8453**, 845317 (2012).
36. J. P. D. Gow and N. J. Murray, "Simplified charge transfer inefficiency correction in CCDs by trap-pumping," *Proc. SPIE* **9915**, 99152A (2016).
37. N. J. Mostek et al., "Charge trap identification for proton-irradiated p+ channel CCDs," *Proc. SPIE* **7742**, 774216 (2010).
38. D. J. Hall et al., "*In situ* trap properties in CCDs: the donor level of the silicon divacancy," *J. Instrum.* **12**(01), P01025 (2017).
39. G. P. Summers et al., "Damage correlations in semiconductors exposed to gamma, electron and proton radiations," *IEEE Trans. Nucl. Sci.* **40**, 1372–1379 (1993).
40. I. Jun et al., "Proton nonionizing energy loss (NIEL) for device applications," *IEEE Trans. Nucl. Sci.* **50**(6), 1891–1895 (2003).
41. M. Mikelsen et al., "Kinetics of divacancy annealing and divacancy-oxygen formation in oxygen-enriched high-purity silicon," *Phys. Rev. B—Condens. Matter Mater. Phys.* **72**, 195207 (2005).
42. D. J. Hall et al., "Determination of *in situ* trap properties in charge coupled devices using a single-trap 'pumping' technique," in *Proc. Eur. Conf. Radiat. and its Effects on Comp. and Syst., RADECS* (2013).
43. G. Seabroke, A. Holland, and M. Cropper, "Modelling radiation damage to ESA's Gaia satellite CCDs," *Proc. SPIE* **7021**, 70211P (2008).
44. S. M. Sze and K. K. Ng, pn Junctions, *Physics of Semiconductor Devices*, Vol. **2**, pp. 80–89, Wiley, New York (2006).
45. M. A. Green, "Intrinsic concentration, effective densities of states, and effective mass in silicon," *J. Appl. Phys.* **67**, 2944–2954 (1990).
46. Y. P. Varshni, "Temperature dependence of the energy gap in semiconductors," *Physica* **34**(1), 149–154 (1967).

Nathan Bush is a postdoctoral scholar at the NASA Jet Propulsion Laboratory working on the flight implementation of EMCCDs for the Roman Coronagraph Instrument. Prior to this, he was a research fellow at the Centre for Electronic Imaging, Open University, UK, where he worked on the development and characterization of customized image sensors for space applications.

David Hall is a lecturer in physical sciences at the Open University. Over the past decade, he has worked on the simulation and analysis of radiation-induced damage to charge transfer in CCDs for the ESA Euclid and Gaia missions, the joint ESA and Chinese Academy of Sciences SMILE mission and NASA's WFIRST mission. He has developed new methods to characterize radiation-induced defects ("traps") in silicon, leading to a more fundamental understanding of how radiation damage affects charge transfer in CCDs.

Andrew Holland is a professor of electro-optics at the Open University, UK, and leads the Centre for Electronic Imaging (CEI). He is an expert in detector physics and has worked on the development of a number of successful space instruments. He has a wealth of knowledge and experience advising on instrument related issues, in particular radiation damage effects and the prediction of orbital performance.